

Optimal Calibration of the endpoint-corrected Hilbert Transform

Eike Osmers^{1,*} and Dorothea Kolossa¹

¹TU Berlin

*Corresponding author: eike.osmers@tu-berlin.de

21st January 2026

Abstract

Accurate, low-latency estimates of the instantaneous phase of oscillations are essential for closed-loop sensing and actuation, including (but not limited to) phase-locked neurostimulation and other real-time applications. The endpoint-corrected Hilbert transform (ecHT) reduces boundary artefacts of the Hilbert transform by applying a causal narrow-band filter to the analytic spectrum. This improves the phase estimate at the most recent sample. Despite its widespread empirical use, the systematic endpoint distortions of ecHT have lacked a principled, closed-form analysis. In this study, we derive the ecHT endpoint operator analytically and demonstrate that its output can be decomposed into a desired positive-frequency term (a deterministic complex gain that induces a calibratable amplitude/phase bias) and a residual leakage term setting an irreducible variance floor. This yields (i) an explicit characterisation and bounds for endpoint phase/amplitude error, (ii) a mean-squared-error-optimal scalar calibration (c-ecHT), and (iii) practical design rules relating window length, bandwidth/order, and centre-frequency mismatch to residual bias via an endpoint group delay. The resulting calibrated ecHT achieves near-zero mean phase error and remains computationally compatible with real-time pipelines. Code and analyses are provided at <https://github.com/eosmers/cechT>.

Contents

1	Introduction	4
1.1	ecHT Algorithm	6
2	Algorithmic Analysis	8
2.1	DFT	8
2.2	Analytic Signal	9
2.3	Filtering	9
2.4	Inverse DFT	10
2.5	Error Analysis	10
2.5.1	Phase	11
2.5.2	Bias-ripple decomposition	12
2.5.3	Error Sources	13
3	Calibration	14
3.1	Calibration for General Complex Signals	14
3.2	Calibration to a Single Tone	17
3.3	Calibration in the Presence of Noise	17
3.4	Calibration Procedure	21
4	Experiments	23
4.1	Simulation	24
4.2	EEG Alpha Phase	25
4.3	Tremor Phase	27
5	Practical Considerations	28
5.1	Window Length	29
5.2	Filter Bandwidth	29
5.3	Filter Order	29
5.4	Centre Frequency Estimate	29
5.5	Sampling Rate, Zero-Padding & Filter Type	30
5.6	DFT Grid	30
6	Discussion	30
6.1	Optimal Calibration	31
6.2	Implications for Closed-Loop Use	32
6.3	Limitations	32
6.4	Outlook	32
6.5	Conclusion	33
7	Code availability	33
8	Author Contributions	33
9	Competing Interests	34

A Notation	39
B Proofs & Derivations	39
B.1 Deterministic phase-ripple and amplitude bounds	39
B.2 Mean-square optimal scalar calibration	41
B.3 Correlation form of the minimal MSE	42
B.4 Bias-variance decomposition	43
B.5 Large-sample properties of the empirical calibration	44
B.6 Optimal scalar calibration for a single tone	48
B.7 Bounding the noise gain	50
C Discussion of argument function	51
C.1 Method 1: phase of the analytic signal	51
C.2 Method 2: phase from the ratio to the original signal	52

1 Introduction

Real-time access to the phase of neural oscillations enables causal experiments and closed-loop stimulation, where stimuli are synchronised with a rhythm’s phase. In neuroscience, this capability is central to closed-loop stimulation paradigms, in which the timing relative to ongoing brain rhythms can be controlled experimentally [1], [2]. More broadly, the same technical requirement arises in any real-time system that must estimate the instantaneous phase of a narrow-band process within tight latency constraints, such as sensing-and-control pipelines, biomedical monitoring, vibration and fault monitoring, and communications-like tracking problems. In all such settings, the estimator must produce a phase estimate within a few milliseconds for each new sample while the signal is still evolving.

The vanilla approach is to construct the analytic signal using the Hilbert transform (HT) and take its argument to determine the instantaneous phase. In discrete-time implementations, this is typically achieved using a discrete Fourier transform (DFT)-based Hilbert transform applied to a short, sliding window. The DFT implicitly assumes that this window repeats periodically. However, when the signal is not exactly periodic across the window, there is a discontinuity between the last and first sample. The Fourier representation of this discontinuity produces Gibbs ringing (overshoot and oscillations), which leads to large amplitude and phase distortions at the window boundaries, as seen in Fig. 1F. As real-time systems usually use only the most recent sample in the window (i.e. the last one) to trigger stimulation, the Gibbs phenomenon directly corrupts the most important estimate.

The endpoint-corrected Hilbert Transform (ecHT) was introduced by Schreglmann et al. [3] as a modification of the classical HT for such online use. The basic idea is to apply a causal, narrow-band bandpass filter to the analytic spectrum centred at the frequency of interest. In the time domain, this filtering reduces the high-frequency components associated with the sharp transition between successive windows. This effectively smooths the periodic continuation of the signal and minimises the Gibbs-induced ringing at the window edges. As the filter is causal and evaluated in a sliding fashion, the ecHT provides a recursive, sample-by-sample phase estimate, with the phase at the last sample of each window being the quantity of interest.

One might try to mitigate boundary artefacts using simpler techniques such as zero-padding or windowing. However, zero-padding moves the discontinuity to the transition between data and padding, and does not systematically reduce the endpoint error. Tapered windows (e.g. Hann) reduce spectral leakage by attenuating the edges of the window; however, in an online setting, they downweight the most recent sample. Symmetric windows or forward-backward filtering can greatly reduce phase distortion, but they require access to future samples and are therefore acausal.

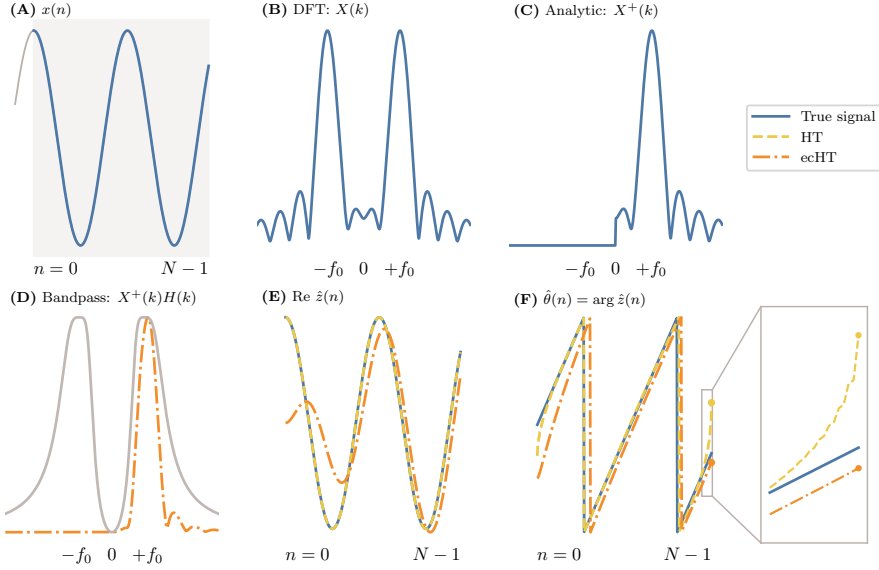


Figure 1: **Visual concept of the ecHT algorithm.** (A) Finite window cut from a longer signal x ; the DFT assumes periodic repetition, creating a discontinuity at the boundaries. (B) DFT magnitude X with positive and negative sidebands. (C) Analytic signal spectrum X^+ after Hilbert mask removes negative frequencies. (D) The ecHT multiplies X^+ with a narrow-band Butterworth response H centred at f_0 . (E) Time-domain real parts: classical Hilbert (orange) shows endpoint ringing; ecHT (yellow) is closer to the true signal (blue). (F) Instantaneous phase near the endpoint: the ecHT reduces the phase error of the online Hilbert transform at the last sample but has itself a bias.

More recently, the ecHT has been applied to the real-time tracking of phases in a variety of biological signals, including essential tremor and alpha or theta rhythms. In these applications, the ecHT has enabled phase-locked stimulation using wearable EEG systems, and has thus served to demonstrate phase-dependent modulation of evoked responses during wakefulness and sleep [4], [5], [6], [7], [8], [9]. Busch et al. [10] observed that the ecHT introduces a distinctive phase shift and Liufu et al. [11] conducted a comprehensive evaluation of the ecHT across various signals. Their study revealed that the ecHT consistently delivers the most accurate and precise phase-locked outputs among several real-time methods. They also found that performance is strongly influenced by signal-to-noise ratio (SNR), amplitude and frequency variability, and window length.

Beyond the ecHT, a variety of other real-time phase estimators have been proposed, including adaptive-filtering approaches [12], [13], waveform-based and spectrogram-based methods [13], [14], [15], state-space models [16], [17], [18],

[19], resonance-based loops [10], [20], [21], [22] and learned predictors [23]. Comparative studies suggest that many of these methods can achieve reliable phase tracking under appropriate conditions [13], [24]. State-space and resonance-based approaches can provide good tracking and handle several non-stationarities, but they typically require model fitting or careful parameter tuning. Spectral and time-frequency methods offer high flexibility across frequencies; however, their finite analysis window introduces a fundamental trade-off between temporal and frequency resolution. Waveform-based predictors also face real-time constraints: filter design and window length must be balanced to achieve an optimal combination of computational speed, latency, and phase-estimation accuracy. Learned predictors can adapt flexibly, but they require substantial training data and are more difficult to analyse theoretically. In this context, ecHT is a low-complexity, FFT-based method that is easy to implement and run in real time. Its errors can be analysed in closed form, as shown below.

Despite its widespread use, previous research into the ecHT has largely been empirical. While existing studies have validated the ecHT experimentally, they have not provided a systematic derivation of its spectral properties, endpoint errors, or calibration strategies. Here, we address this issue. We provide an analytical DFT-based characterisation of the endpoint-corrected Hilbert transform, express its error analytically, and demonstrate how a single scalar can deliver a mean-squared-error (MSE)-optimal calibration. We refer to the calibrated variant of the ecHT as the *c-ecHT*. We then translate these results into practical design rules concerning window length, filter bandwidth and order, and centre-frequency estimation. These rules allow the ecHT to achieve real-time phase estimates with mean errors of practically zero degrees under realistic conditions, as confirmed in simulations and neural data.

The remainder of the paper is organised as follows. Section 1.1 specifies the ecHT algorithm and notation. Section 2 provides a DFT-based analysis of the ecHT pipeline and derives an explicit endpoint error characterisation. Section 3 develops the MSE-optimal scalar calibration and its estimators. The theory is evaluated in simulations in Section 4 and practical recommendations and limitations are discussed in Section 5.

1.1 ecHT Algorithm

The ecHT is based on the analytic signal representation of a narrow-band real-valued signal. Let x denote a discrete-time signal that is approximately band-limited around a centre frequency f_0 (e.g. a tremor or alpha rhythm). Its analytic signal is defined as

$$z(n) = x(n) + j\mathcal{H}x(n) \quad (1.6)$$

where \mathcal{H} denotes the Hilbert transform. The Hilbert transform constructs a quadrature counterpart to x , where z encodes the instantaneous amplitude and

Algorithm 1 endpoint-corrected Hilbert Transform (ecHT)

Input: Discrete-time signal $x(n)$, centre frequency f_0 , bandpass filter H

Output: Estimated instantaneous phase $\hat{\theta}(n)$

1: Compute the discrete Fourier transform (DFT) of the input signal

$$X(k) \leftarrow \text{DFT}\{x(n)\} \quad (1.1)$$

2: Construct the analytic spectrum $X^+(k)$, with \mathcal{P} denoting the set of positive DFT frequency indices

$$X^+(k) \leftarrow 2X(k)\mathbf{1}_{k \in \mathcal{P}}, \quad X^+(0) \leftarrow X(0) \quad (1.2)$$

3: Apply bandpass filter around the centre frequency f_0

$$\hat{Z}(k) \leftarrow X^+(k)H(k) \quad (1.3)$$

4: Compute the inverse DFT to obtain the analytic signal estimate

$$\hat{z}(n) \leftarrow \text{iDFT}\{\hat{Z}(k)\} \quad (1.4)$$

5: Extract instantaneous phase

$$\hat{\theta}(n) \leftarrow \arg \hat{z}(n) \quad (1.5)$$

6: **return** $\hat{\theta}(n)$

phase. The instantaneous phase is then

$$\theta = \arg z(n) = \arctan2(\text{Im } z(n), \text{Re } z(n)) = \arctan2(\text{Im } z(n), x(n)). \quad (1.7)$$

In the ecHT, this analytic signal is computed in short windows of length N using the DFT. For each new sample, a window $\{x(0), \dots, x(N-1)\}$ is analysed, and only the phase of the last sample $\theta(N-1)$ is used. This endpoint-focused, sliding-window evaluation is what makes the ecHT an online algorithm: it can be implemented recursively and updated sample by sample, without requiring access to future data, while keeping latency low.

The key modification relative to the standard DFT-based Hilbert transform is the introduction of a bandpass filter around the frequency of interest f_0 in the frequency domain. After forming the analytic spectrum X^+ by zeroing the negative DFT bins and doubling the positive ones, the ecHT multiplies X^+ by the frequency response H of a causal narrow-band filter centred at f_0 :

$$\tilde{Z}(k) = X^+(k)H(k) \quad (1.8)$$

In the time domain, this corresponds to convolving the analytic signal with a causal bandpass filter that selectively preserves components near f_0 while attenuating others. Importantly, this operation smooths the abrupt jump between

the last and first samples introduced by the rectangular window, thereby reducing Gibbs ringing and endpoint distortion. The inverse DFT of \hat{Z} yields the ecHT approximation \hat{z} , and the ecHT phase estimate is

$$\hat{\theta}(n) = \arg \hat{z}(n). \quad (1.9)$$

Algorithm 1 summarises these steps. Using FFT-based implementations, the computational complexity is $\mathcal{O}(L \log L)$ per window, and the filter can be implemented recursively, meaning that only the most recent sample needs updating. For the remainder of the paper, we will denote the true mathematical analytic signal by z , and its ecHT-based estimate at the endpoint by \hat{z} . We will focus on analysing and calibrating the phase error $\hat{\theta}(N-1) - \theta(N-1)$ which is most relevant for real-time closed-loop applications.

2 Algorithmic Analysis

The ecHT algorithm is analysed using the DFT. The DFT implicitly assumes a rectangular window around the signal with periodic extension. Hence, a jump discontinuity manifests at the signal's edge in the absence of periodicity, thereby inducing the Gibbs phenomenon and leakage in time domain. As demonstrated in Fig. 1B, this DFT window forms a Dirichlet kernel in frequency domain, characterised by the presence of pronounced side lobes. This manifests in spectral leakage.

Assuming a finite length real cosine signal

$$\begin{aligned} x(n) &= \cos(\omega_0 n + \varphi_0) \quad n = 0, \dots, N-1 \\ &= \frac{1}{2} \left(e^{j(\omega_0 n + \varphi_0)} + e^{-j(\omega_0 n + \varphi_0)} \right) \end{aligned} \quad (2.1)$$

sampled at F_s .

$$\omega_0 = \frac{2\pi f_0}{F_s} \quad (2.2)$$

Outside $[0, N-1]$ the signal is windowed to be zero.

2.1 DFT

The L -point DFT of x can be expressed through the discrete frequencies $\omega_k = 2\pi k/L$, where $k = 0, \dots, L-1$ corresponds to the DFT bin frequency. If $L > N$ assume x to be zero-padded to length L .

Defining the length- N Dirichlet kernel D_N [25] as

$$D_N(\omega) = \sum_{n=0}^{N-1} e^{j\omega n} = e^{j\omega \frac{N-1}{2}} \frac{\sin \frac{N\omega}{2}}{\sin \frac{\omega}{2}}, \quad (2.3)$$

the DFT of the signal can be expressed through the Dirichlet kernel compactly

$$\begin{aligned}
X(k) &= \sum_{n=0}^{N-1} x(n) e^{-j \frac{2\pi k n}{L}}, \quad \omega_k = \frac{2\pi k}{L} \\
&= \frac{1}{2} \sum_{n=0}^{N-1} \left(e^{j(\omega_0 n + \varphi_0)} + e^{-j(\omega_0 n + \varphi_0)} \right) e^{-j\omega_k n} \\
&= \frac{1}{2} \left[e^{j\varphi_0} \sum_{n=0}^{N-1} e^{-j(\omega_k - \omega_0)n} + e^{-j\varphi_0} \sum_{n=0}^{N-1} e^{-j(\omega_k + \omega_0)n} \right] \\
&= \frac{1}{2} e^{j\varphi_0} D_N(\omega_0 - \omega_k) + \frac{1}{2} e^{-j\varphi_0} D_N(-\omega_0 - \omega_k) \\
&= X_+(k) + X_-(k),
\end{aligned} \tag{2.4}$$

with X_+ representing the positive frequency lobe near ω_0 and X_- the negative frequency lobe near $-\omega_0$. The positive main peak of the Dirichlet kernel characterising the analytic harmonic function will appear at k_0 , which is the index of the bin closest to ω_0 .

$$k_0 = \arg \min_k |\omega_0 - \omega_k| \tag{2.5}$$

2.2 Analytic Signal

Ideally, the analytic signal would be obtained by completely suppressing the negative-frequency component X_- , but X_- , which is nonzero almost everywhere, cannot be removed exactly. Instead, the analytic signal is approximated by applying an analytic mask, which sets the negative-frequency DFT bins to zero and doubles the positive-frequency bins. However, residual leakage of X_- into the positive-frequency region remains, introducing a bias in the phase estimate.

$$m(k) = \begin{cases} 1 & k = 0 \\ 2 & 1 \leq k \leq \lfloor L/2 \rfloor - 1 \\ 1 & k = L/2 \text{ (if } L \text{ is even)} \\ 0 & \text{otherwise} \end{cases} \tag{2.6}$$

2.3 Filtering

Let H denote the frequency response of a causal bandpass filter centred on the frequency of interest. Multiplying the analytic spectrum by this response

$$\hat{Z}(k) = H_{\text{eff}}(k)X(k), \quad H_{\text{eff}}(k) = m(k)H(k) \tag{2.7}$$

applies the desired narrow-band filter in the frequency domain. In practice, H is obtained numerically using standard filter design tools evaluated at DFT frequencies; its closed-form expression is not required for the subsequent analysis.

2.4 Inverse DFT

The inverse DFT yields the analytic signal \hat{z} .

$$\hat{z}(n) = \frac{1}{L} \sum_{k=0}^{L-1} \hat{Z}(k) e^{jn\omega_k} \quad (2.8)$$

Evaluating (2.8) at the last sample $\hat{z}(N-1) = \hat{z}_{\text{end}}$ as the ecHT algorithm is called recursively to estimate the phase of newest sample.

$$\begin{aligned} \hat{z}_{\text{end}} &= \frac{1}{L} \sum_{k=0}^{L-1} H_{\text{eff}}(k) X_+(k) e^{j\omega_k(N-1)} + \frac{1}{L} \sum_{k=0}^{L-1} H_{\text{eff}}(k) X_-(k) e^{j\omega_k(N-1)} \\ &= \frac{1}{2L} e^{j\varphi_0} \sum_{k=0}^{L-1} H_{\text{eff}}(k) D_N(\omega_0 - \omega_k) e^{j\omega_k(N-1)} \\ &\quad + \frac{1}{2L} e^{-j\varphi_0} \sum_{k=0}^{L-1} H_{\text{eff}}(k) D_N(-\omega_0 - \omega_k) e^{j\omega_k(N-1)} \end{aligned} \quad (2.9)$$

We can now define the lumped positive-frequency contribution and negative-frequency contribution

$$\hat{Z}_+ = \frac{1}{2L} \sum_{k=0}^{L-1} H_{\text{eff}}(k) D_N(\omega_0 - \omega_k) e^{j\omega_k(N-1)} \quad (2.10)$$

$$\hat{Z}_- = \frac{1}{2L} \sum_{k=0}^{L-1} H_{\text{eff}}(k) D_N(-\omega_0 - \omega_k) e^{j\omega_k(N-1)} \quad (2.11)$$

$$\hat{z}_{\text{end}} = e^{j\varphi_0} \hat{Z}_+ + e^{-j\varphi_0} \hat{Z}_-, \quad (2.12)$$

which incorporate finite window truncation due to the Dirichlet kernel effect D_N and the analytic signal half-spectrum by application of the mask m . Additionally, they encapsulate the bandpass filter shape and time index shift to $n = N - 1$ (the phase factor $e^{j\omega_k(N-1)}$).

2.5 Error Analysis

When designing a causal ecHT, it is unavoidable that there will be a trade-off between amplitude and phase accuracy. In this section, we characterise the endpoint error induced by finite windowing (i.e. the Dirichlet kernel), analytic masking, and bandpass filtering. All deterministic endpoint effects will be captured by a single complex gain factor.

For a length- N cosine $x(n) = \cos(\omega_0 n + \varphi_0)$ we use the ideal analytic reference at the newest sample

$$z_{\text{end}} = z(N-1) = e^{j(\omega_0(N-1) + \varphi_0)}, \quad (2.13)$$

and compare the ecHT endpoint estimate \hat{z}_{end} against it. We define the endpoint gain

$$F = \frac{\hat{z}_{\text{end}}}{z_{\text{end}}}, \quad (2.14)$$

whose argument and magnitude directly encode phase and amplitude errors:

$$\varepsilon_\theta = \arg\{\hat{z}_{\text{end}}\} - \arg\{z_{\text{end}}\} = \arg F \quad (2.15)$$

$$\varepsilon_A = |\hat{z}_{\text{end}}| - 1 = |F| - 1. \quad (2.16)$$

In the ideal case $F = 1$ so that $\varepsilon_\theta = \varepsilon_A = 0$.

The ecHT endpoint can be written as a superposition of a positive-frequency and a negative-frequency contribution. After factoring out the reference phase $e^{j\omega_0(N-1)}$, this yields

$$\begin{aligned} F &= \frac{\hat{Z}_+ e^{j\varphi_0} + \hat{Z}_- e^{-j\varphi_0}}{e^{j(\omega_0(N-1)+\varphi_0)}} \\ &= e^{-j\omega_0(N-1)} \left(\hat{Z}_+ + \hat{Z}_- e^{-j2\varphi_0} \right) \\ &= G_+ + G_- e^{-j2\varphi_0}, \end{aligned} \quad (2.17)$$

where

$$\begin{aligned} G_+ &= \hat{Z}_+ e^{-j\omega_0(N-1)} \\ &= \frac{1}{2L} e^{-j\omega_0(N-1)} \sum_{k=0}^{L-1} H_{\text{eff}}(k) D_N(\omega_0 - \omega_k) e^{j\omega_k(N-1)}, \end{aligned} \quad (2.18)$$

$$\begin{aligned} G_- &= \hat{Z}_- e^{-j\omega_0(N-1)} \\ &= \frac{1}{2L} e^{-j\omega_0(N-1)} \sum_{k=0}^{L-1} H_{\text{eff}}(k) D_N(-\omega_0 - \omega_k) e^{j\omega_k(N-1)}. \end{aligned} \quad (2.19)$$

G_+ is the deterministic complex gain of the implemented ecHT endpoint operator at ω_0 , incorporating the effects of a finite window, the analytic mask, and the sampled bandpass response. We denote its unwrapped phase by $\alpha(\omega) = \text{unwrap}(\arg G_+)$. G_- quantifies the residual negative-frequency leakage that is passed by the effective analytic mask and filter. Notably, G_+ is independent of φ_0 , whereas the leaked term inherits a φ_0 -dependent rotation.

2.5.1 Phase

Instantaneous phase is taken as the argument of the (estimated) analytic signal

$$\hat{\theta}(n) = \arg \hat{z}(n) = \text{arctan2}(\text{Im } \hat{z}_{\text{end}}, \text{Re } \hat{z}_{\text{end}}). \quad (2.20)$$

At the endpoint we have the factorisation $\hat{z}_{\text{end}} = z_{\text{end}} F$, where F collects the deterministic effects of finite windowing, analytic masking, and bandpass filtering

and $z_{\text{end}} = e^{j(\omega_0(N-1)+\varphi_0)}$ is the ideal analytic endpoint of the tone. Therefore the endpoint phase estimate satisfies

$$\hat{\theta}(N-1) = \arg \hat{z}_{\text{end}} = \arg \{z_{\text{end}} F\} = \omega_0(N-1) + \varphi_0 + \arg F, \quad (2.21)$$

so all systematic distortions enter additively via $\arg F$, enabling the bias-ripple decomposition in Sec. 2.5.2.

The literature offers an apparently equivalent alternative that replaces the real part of the sample-based estimate $\text{Re } \hat{z}(n)$ with the original real sample $x(n)$ in the denominator. While this matches the phase of the ideal analytic signal $\arg z(n)$ (because $\text{Re } z(n) = x(n)$), it is not equivalent for ecHT: the effective gain $F = F_R + jF_I$ rotates and rescales the quadrature pair, yielding $\tan \hat{\theta}(N-1) = F_R \tan(\omega_0(N-1) + \varphi_0) + F_I$, i.e. a φ_0 - and time-dependent phase warping even for a single tone. See Appendix C for the full discussion. For this reason, we use (2.20) exclusively throughout.

2.5.2 Bias-ripple decomposition

Define the leakage ratio r

$$G_+ = |G_+| e^{j\alpha}, \quad G_- = |G_-| e^{j\beta}, \quad r = \frac{|G_-|}{|G_+|}, \quad \Delta = \beta - \alpha. \quad (2.22)$$

Then

$$F(\varphi_0) = |G_+| e^{j\alpha} \left(1 + r e^{j(\Delta - 2\varphi_0)} \right). \quad (2.23)$$

This motivates splitting the total phase error into a deterministic (calibratable) bias and a φ_0 -dependent leakage ripple.

$$\varepsilon_\theta(\varphi_0) = \arg F = \alpha + \delta_\theta(\varphi_0), \quad \delta_\theta(\varphi_0) = \arg F(\varphi_0) - \arg G_+ \quad (2.24)$$

Similarly, the amplitude error decomposes into a deterministic amplitude bias controlled by $|G_+|$ and a φ_0 -dependent modulation induced by G_- .

If the centre frequency shifts $\omega = \omega_0 + \Delta\omega$, then the deterministic bias term changes as

$$\alpha(\omega_0 + \Delta\omega) \approx \alpha(\omega_0) - \Delta\omega \tau_g(\omega_0). \quad (2.25)$$

The group delay is defined here as

$$\tau_g(\omega) = -\frac{d}{d\omega} \alpha(\omega), \quad \alpha(\omega) = \text{unwrap}(\arg G_+) \quad (2.26)$$

as the phase slope of the endpoint gain G_+ in (2.18), not necessarily the group delay of the prototype filter H alone.

Theorem 1 (Deterministic phase-ripple and amplitude bounds, Proof Appendix B.1). *Assume $|G_-| \leq |G_+|$ and define $r \in [0, 1]$ and $\alpha = \arg G_+$ as above. Let*

$$F(\varphi_0) = G_+ + G_- e^{-j2\varphi_0}, \quad \delta_\theta(\varphi_0) = \arg\{F(\varphi_0)\} - \alpha. \quad (2.27)$$

Then for all $\varphi_0 \in \mathbb{R}$,

$$|\delta_\theta(\varphi_0)| \leq \arcsin r. \quad (2.28)$$

Moreover, the amplitude error satisfies the uniform bound

$$|\varepsilon_A(\varphi_0)| = |F(\varphi_0)| - 1 \leq |G_+| - 1 + |G_-|. \quad (2.29)$$

A scalar calibration can remove the deterministic bias encoded in G_+ , whereas G_- produces phase and amplitude ripples that vary with φ_0 and therefore set a deterministic worst-case floor. Consequently, if the filter successfully suppresses most of the negative-frequency component (e.g. $r = 0.1$), the maximum possible phase error after calibrating α at the newest sample is $\arcsin(0.1) \approx 5.7^\circ$. In practice, typical leakage ratios are on the order of a few percent, yielding only a few degrees of worst-case bias. This has been validated in Section 4.1.

For $r \ll 1$,

$$\delta_\theta(\varphi_0) = \arg\left\{1 + r e^{j(\Delta - 2\varphi_0)}\right\} \approx r \sin(\Delta - 2\varphi_0), \quad (2.30)$$

so the phase error is well-approximated by a constant bias α plus a small sinusoidal wobble with period π in φ_0 . The endpoint magnitude is

$$\begin{aligned} |F(\varphi_0)| &= |G_+| \sqrt{1 + r^2 + 2r \cos(\Delta - 2\varphi_0)} \\ &\approx |G_+| \left(1 + r \cos(\Delta - 2\varphi_0)\right), \end{aligned} \quad (2.31)$$

so ε_A contains a constant part $|G_+| - 1$ and a small oscillatory part due to leakage.

2.5.3 Error Sources

The endpoint error can be understood in terms of the complex gain $F = G_+ + G_- e^{-j2\varphi_0}$ introduced in Section 2.5. G_+ is independent of the initial phase φ_0 and acts as a constant complex gain at the frequency of interest. Its argument produces a constant phase bias α , whose local frequency sensitivity is governed by the endpoint group delay $\tau_g(\omega_0)$ of (2.26). This component is fully deterministic for a given eHT design and can therefore be removed by a global complex calibration factor.

The second term, $G_- e^{-j2\varphi_0}$ arises from negative-frequency leakage through the Dirichlet kernel and generates a phase and amplitude ripple around the aforementioned bias. As it depends on φ_0 , it varies from cycle to cycle (even for

identical noise conditions) and contributes to the variance of the endpoint error rather than its mean. In the small-leakage regime, this produces a sinusoidal wobble of the phase error in (2.30) with amplitude proportional to the leakage ratio $r = |G_-|/|G_+|$.

This bias-variance dichotomy is made explicit in the MSE decomposition and calibration results of Section 3 and Appendix B.4: scalar calibration can eliminate the bias associated with G_+ , but the variance floor set by G_- and by noise remains, and must be controlled through design choices such as window length, bandwidth and filter order.

The analysis depends on the assumed centre frequency f_0 because both H and, consequently $G_{+,-}$ are dependent on the centring of the bandpass. If the true instantaneous frequency is $f(t) = f_0 + \Delta f(t)$, then $G_+(f)$ is sampled off-centre and its argument becomes time-varying, resulting in a time-varying phase bias even after applying a fixed calibration. As seen in (2.25), this mismatch induces a bias proportional to the group delay $\Delta\omega\tau_g(\omega_0)$, motivating online tracking of f_0 and periodic re-computation of the frequency-specific calibration when drift is present.

3 Calibration

The previous section characterised the deterministic complex gain induced by windowing and filtering at the endpoint F . This section shows that a single complex scalar can be used to calibrate the ecHT endpoints to minimise mean-square error with respect to an ideal analytic reference, first in general and then for a single tone.

3.1 Calibration for General Complex Signals

Let Z denote the ideal analytic signal endpoint on a window, and let \hat{Z} denote the corresponding ecHT endpoint estimate on the same window. We model (Z, \hat{Z}) as a pair of complex-valued random variables capturing variability across repeated windows/trials (e.g. due to noise, phase, and mild non-stationarity). Expectations below are understood as limits over such repetitions.

We introduce a complex scalar calibration factor $C \in \mathbb{C}$ to compensate for both amplitude bias (through $|C|$) and systematic phase offset (through $\arg C$).

$$\hat{z}_C(n) = C\hat{z}(n), \quad \hat{Z}_C = C\hat{Z} \quad (3.1)$$

Calibration quality is measured by the mean-square error (MSE).

$$J(C) = \mathbb{E} \left[|C\hat{Z} - Z|^2 \right] \quad (3.2)$$

Theorem 2 (Mean-square optimal scalar calibration, Proof Appendix B.2). *Let Z, \hat{Z} be complex random variables with finite second moments and $\mathbb{E}[|\hat{Z}|^2] > 0$. Then $J(C)$ in (3.2) is strictly convex in $C \in \mathbb{C}$ and attains its unique minimum at*

$$C_{\text{opt}} = \frac{\mathbb{E}[\hat{Z}^* Z]}{\mathbb{E}[|\hat{Z}|^2]}. \quad (3.3)$$

The corresponding minimal mean-square error is

$$J(C_{\text{opt}}) = \mathbb{E}[|Z|^2] - \frac{|\mathbb{E}[\hat{Z}^* Z]|^2}{\mathbb{E}[|\hat{Z}|^2]} \leq J(1) = \mathbb{E}[|\hat{Z} - Z|^2], \quad (3.4)$$

so an optimally chosen scalar calibration never increases the MSE relative to the uncalibrated estimate.

C_{opt} in (3.3) aligns the phase of \hat{Z} to Z and scales the amplitude, essentially correcting the systematic bias. Thus, C_{opt} is the unique scalar calibration that minimises $J(C)$ and has the structure of a complex Wiener filter. It is the scalar linear estimator mapping \hat{Z} to the best linear mean-square estimate of Z .

To express the minimal MSE in terms of correlation, assume $\mathbb{E}[|Z|^2] > 0$ and define the complex correlation coefficient

$$\rho_{Z\hat{Z}} = \frac{\mathbb{E}[\hat{Z}^* Z]}{\sqrt{\mathbb{E}[|\hat{Z}|^2]\mathbb{E}[|Z|^2]}}. \quad (3.5)$$

Corollary 1 (Correlation form of the minimal MSE, Proof Appendix B.3). *With $\rho_{Z\hat{Z}}$ as above,*

$$J(C_{\text{opt}}) = \mathbb{E}[|Z|^2] \left(1 - |\rho_{Z\hat{Z}}|^2\right), \quad (3.6)$$

with $0 \leq J(C_{\text{opt}}) \leq \mathbb{E}[|Z|^2]$. Moreover,

- $J(C_{\text{opt}}) = 0$ if and only if $\hat{Z} = CZ$ almost surely (perfect linear predictability);
- $J(C_{\text{opt}}) = \mathbb{E}[|Z|^2]$ if and only if \hat{Z} and Z are uncorrelated, i.e. $\mathbb{E}[\hat{Z}^* Z] = 0$.

Geometrically, $C_{\text{opt}}\hat{Z}$ is the orthogonal projection of Z onto the one-dimensional subspace spanned by \hat{Z} in the Hilbert space of complex random variables. The factor $|\rho_{Z\hat{Z}}|^2$ is the fraction of analytic-signal energy that can be recovered linearly from the ecHT endpoint, while $1 - |\rho_{Z\hat{Z}}|^2$ quantifies the loss that is not recoverable due to filtering, windowing, and spectral leakage. Calibration can only recover information present in \hat{Z} ; it cannot undo distortions that are uncorrelated with Z .

It is also helpful to separate bias and variability which is derived in Appendix B.4.

$$J(C) = \left| \mathbb{E}[C\hat{Z} - Z] \right|^2 + \mathbb{E} \left[|(C\hat{Z} - Z) - \mathbb{E}[C\hat{Z} - Z]|^2 \right] \quad (3.7)$$

The MSE can be decomposed into squared bias term and variance terms. The bias captures systematic distortions, while the variance measures inconsistency between cycles caused by noise and phase-dependent leakage. The optimal calibration C_{opt} minimises both contributions jointly; any further improvement requires a reduction in leakage or noise in the ecHT itself, rather than relying on additional rescaling.

In practice, C_{opt} is unknown and must be estimated from data. Suppose we have M windows or trials yielding pairs (Z_i, \hat{Z}_i) , $i = 0, \dots, M-1$, at a fixed endpoint. A natural empirical estimator is

$$\hat{C}_M = \frac{\sum_{i=0}^{M-1} \hat{Z}_i^* Z_i}{\sum_{i=0}^{M-1} |\hat{Z}_i|^2}. \quad (3.8)$$

Corollary 2 (Large-sample properties of the empirical calibration, Proof Appendix B.5). *Assume that the sequence $\{(Z_i, \hat{Z}_i)\}_{i \geq 1}$ is strictly stationary and weakly dependent, with finite moments of order $2 + \delta$ for some $\delta > 0$. Then the estimator \hat{C}_M in (3.8) satisfies:*

1. Consistency: $\hat{C}_M \rightarrow C_{\text{opt}}$ almost surely as $M \rightarrow \infty$;
2. Asymptotic normality: $\sqrt{M}(\hat{C}_M - C_{\text{opt}}) \rightarrow \mathcal{N}_{\mathbb{C}}(\mathbf{0}, \Sigma)$ for some covariance matrix Σ .

Thus, averaging over more windows or repetitions yields a calibration coefficient that converges to the theoretical optimum at the usual $1/\sqrt{M}$ rate.

Corollary 2 provides a general, data-driven scheme for learning a global, complex gain by regressing the ecHT output onto a reference analytic signal. The theorem guarantees that this empirical gain asymptotically converges to the MSE-optimal scalar as the calibration window increases. However, in the short-window, near-single-tone regime considered here, where f_0 is known or can be accurately estimated, and where an accurate analytic expression for the endpoint error is available, the closed-form calibration in Section 3.2 is both more efficient and more reliable. Data-driven calibration can converge slowly and depend critically on the quality of the reference, potentially degrading endpoint performance if fitted to short windows. Corollary 2 can be viewed primarily as providing a theoretical and practical extension for more complex pipelines (e.g. broader-band or hardware-perturbed signals), where analytic endpoint characterisations are unavailable, but ample calibration data is accessible.

3.2 Calibration to a Single Tone

Now, these results are specialised to a finite-length cosine analysed in Section 2.5. In that case the eHT endpoint can be written as

$$F = \frac{\hat{z}_{\text{end}}}{z_{\text{end}}} = G_+ + G_- e^{-j2\varphi_0}, \quad (3.9)$$

where G_+ is the complex gain for the positive-frequency component, G_- is the (typically small) gain for the negative-frequency component (leakage), and φ_0 is the unknown initial phase. The phase is modelled by $\varphi_0 \sim \mathcal{U}(-\pi, \pi)$ to represent arbitrary phase across repetitions, and the ideal analytic endpoint is normalised to $|Z| = 1$.

Using $\mathbb{E}[e^{\pm j2\varphi_0}] = 0$, it follows that

$$\mathbb{E}[\hat{Z}^* Z] = G_+^*, \quad \mathbb{E}[|\hat{Z}|^2] = |G_+|^2 + |G_-|^2. \quad (3.10)$$

Theorem 3 (Optimal scalar calibration for a single tone, Proof Appendix B.6). *Under the assumptions above, the MSE-optimal scalar calibration factor (3.3) reduces to*

$$C_{\text{opt}} = \frac{G_+^*}{|G_+|^2 + |G_-|^2}, \quad (3.11)$$

and the corresponding minimal MSE is

$$J(C_{\text{opt}}) = \frac{|G_-|^2}{|G_+|^2 + |G_-|^2}. \quad (3.12)$$

In other words, the irreducible error after optimal calibration equals the fraction of negative-frequency leakage power in the total eHT endpoint power.

From (3.11), (3.12) the correlation coefficient is also obtained

$$\rho_{Z\hat{Z}} = \frac{G_+^*}{\sqrt{|G_+|^2 + |G_-|^2}}, \quad |\rho_{Z\hat{Z}}|^2 = \frac{|G_+|^2}{|G_+|^2 + |G_-|^2}, \quad (3.13)$$

where G_+^* is the complex conjugate of G_+ . So, in the single-tone case the recoverable signal fraction is determined by the ratio of main-lobe gain to total power, and calibration cannot correct the portion of energy that has leaked from the negative frequency.

3.3 Calibration in the Presence of Noise

Let the pure tone be noisy

$$x(n) = s(n) + \eta(n), \quad (3.14)$$

where $s(n)$ is the finite-length single tone and $\eta(n)$ is zero-mean noise with $\mathbb{E}[|\eta(n)|^2] = \sigma_\eta^2$. We normalise the analytic signal such that $|Z| = 1$ at the endpoint, so that the input SNR is

$$\text{SNR}_{\text{in}} = \frac{\mathbb{E}[|s(n)|^2]}{\mathbb{E}[|\eta(n)|^2]} = \frac{1}{\sigma_\eta^2}. \quad (3.15)$$

By linearity of the ecHT the complex-valued noise contribution W gets added to the estimate,

$$\hat{Z} = FZ + W, \quad (3.16)$$

where $F = G_+ + G_- e^{-j2\varphi_0}$ and $\varphi_0 \sim \mathcal{U}(-\pi, \pi)$. $G_{\text{noise}} > 0$ is the noise gain of the ecHT endpoint.

$$\sigma_W^2 = \mathbb{E}[|W|^2] = G_{\text{noise}} \sigma_\eta^2 \quad (3.17)$$

It can be pre-computed once from the impulse response for a given design. Assuming W is independent of φ_0 and Z , the single-tone analysis (3.11) yields

$$\mathbb{E}[\hat{Z}^* Z] = \mathbb{E}[F^*] = G_+^*, \quad (3.18)$$

$$\mathbb{E}[|\hat{Z}|^2] = \mathbb{E}[|F|^2] + \mathbb{E}[|W|^2] = |G_+|^2 + |G_-|^2 + \sigma_W^2. \quad (3.19)$$

The MSE-optimal correction factor in the presence of noise is therefore

$$C_{\text{opt}} = \frac{\mathbb{E}[\hat{Z}^* Z]}{\mathbb{E}[|\hat{Z}|^2]} = \frac{G_+^*}{|G_+|^2 + |G_-|^2 + \sigma_W^2}. \quad (3.20)$$

In practice σ_W^2 is usually unknown. If a calibration segment with a known tone is available, σ_W^2 can be estimated; otherwise a robust choice is the deterministic (noise-free) solution

$$C_{\text{det}} = \frac{G_+^*}{|G_+|^2 + |G_-|^2}, \quad (3.21)$$

which is optimal for the noiseless model and remains near-optimal at moderate SNR.

Define the signal-to-noise ratio at the ecHT endpoint as

$$\text{SNR}_{\text{out}} = \frac{\mathbb{E}[|FZ|^2]}{\mathbb{E}[|W|^2]}. \quad (3.22)$$

Since $|Z| = 1$ and $\mathbb{E}[|F|^2] = |G_+|^2 + |G_-|^2$ from (B.63), this becomes

$$\text{SNR}_{\text{out}} = \frac{|G_+|^2 + |G_-|^2}{\sigma_W^2} = \frac{|G_+|^2 + |G_-|^2}{G_{\text{noise}} \sigma_\eta^2} = G_{\text{SNR}} \text{SNR}_{\text{in}}, \quad (3.23)$$

$$G_{\text{SNR}} = \frac{|G_+|^2 + |G_-|^2}{G_{\text{noise}}} \quad (3.24)$$

Thus, for a fixed ecHT design, the output SNR scales linearly with the input SNR. By Cauchy-Schwarz, the endpoint noise gain is bounded from below by the main- and leakage-gain as derived in Appendix B.7

$$G_{\text{noise}} \geq \frac{|G_+|^2 + |G_-|^2}{2N} \gtrsim \frac{|G_+|^2}{2N}. \quad (3.25)$$

It shows that the ecHT cannot simultaneously achieve large single-tone gain and arbitrarily low noise: improving signal gain inevitably sets a lower bound on the endpoint noise power.

To relate the complex-domain error to phase error, consider the calibrated endpoint estimate

$$Z_{\text{cal}} = C_{\text{det}} \hat{Z}, \quad (3.26)$$

with true analytic endpoint Z and residual error

$$\varepsilon = Z_{\text{cal}} - Z = (C_{\text{det}} F - 1)Z + C_{\text{det}} W, \quad (3.27)$$

The minimal mean-square error after deterministic calibration using (3.9), (3.21) and (3.23) is

$$J = J(C_{\text{det}}) = \mathbb{E}[|\varepsilon|^2] = \mathbb{E}[|C_{\text{det}} F - 1|^2] + |C_{\text{det}}|^2 \sigma_W^2 = \ell + \frac{1 - \ell}{\text{SNR}_{\text{out}}}, \quad (3.28)$$

$$\ell = \frac{|G_-|^2}{|G_+|^2 + |G_-|^2}, \quad (3.29)$$

so that, in particular, $J \approx 1/\text{SNR}_{\text{out}}$ for $\ell \approx 0$.

Let $\theta = \arg Z$ denote the true phase at the endpoint and $\hat{\theta} = \arg Z_{\text{cal}}$ the c-ecHT phase estimate, with phase error

$$\Delta\theta = \hat{\theta} - \theta. \quad (3.30)$$

Without loss of generality the complex plane may be rotated such that $Z = 1$, i.e. $Z_{\text{cal}} = 1 + \tilde{\varepsilon}$, where $\tilde{\varepsilon} = \varepsilon/Z$ has the same squared magnitude as ε . For small errors $|\tilde{\varepsilon}| \ll 1$, the geometry of the complex plane gives

$$\Delta\theta \approx \text{Im}\{\tilde{\varepsilon}\}. \quad (3.31)$$

Since $|\tilde{\varepsilon}|^2 = (\text{Re } \tilde{\varepsilon})^2 + (\text{Im } \tilde{\varepsilon})^2$ and $J = \mathbb{E}[|\tilde{\varepsilon}|^2]$, an approximately isotropic error distribution implies

$$\mathbb{E}[(\text{Re } \tilde{\varepsilon})^2] \approx \mathbb{E}[(\text{Im } \tilde{\varepsilon})^2] \approx \frac{J}{2}, \quad (3.32)$$

and therefore the phase variance is

$$\sigma_\theta^2 = \mathbb{E}[\Delta\theta^2] \approx \frac{J}{2}. \quad (3.33)$$

And the phase standard deviation is obtained using (3.28).

$$\sigma_\theta [\text{deg}] \approx \frac{180}{\pi} \sqrt{\frac{1}{2} \left[\ell + \frac{1-\ell}{G_{\text{SNR}} \text{SNR}_{\text{in}}} \right]} \approx \frac{180}{\pi} \sqrt{\frac{1}{2G_{\text{SNR}} \text{SNR}_{\text{in}}}} \quad (3.34)$$

The above derivation relies on two approximations: a small-error regime $|\tilde{\varepsilon}| \ll 1$, and an approximately isotropic error distribution. Consequently, the resulting expression for the phase variance is only expected to be accurate only when the endpoint SNR is sufficiently high and the residual error distribution is close to circularly symmetric in the complex plane. In particular, the approximation tends to slightly underestimate the true phase standard deviation at low SNR, as illustrated in Table 1.

After deterministic calibration and rotation we work with the normalised endpoint estimate

$$Z_{\text{cal}} = 1 + \varepsilon, \quad \Phi = \arg(Z_{\text{cal}}) = \arg(1 + \varepsilon), \quad (3.35)$$

where the complex residual ε has zero mean and second moment

$$J = \mathbb{E}[|\varepsilon|^2]. \quad (3.36)$$

In the regime where the residual is approximately isotropic we model it as a circular complex Gaussian,

$$\varepsilon \sim \mathcal{N}_{\mathbb{C}}(0, J), \quad \text{Re } \varepsilon, \text{Im } \varepsilon \sim \mathcal{N}(0, J/2). \quad (3.37)$$

This assumption removes the small-error linearisation while keeping the empirically testable isotropy/properness condition.

Let $Z_{\text{cal}} = X + jY$ with (X, Y) jointly Gaussian where \mathbf{I} denotes the 2×2 identity matrix.

$$(X, Y) \sim \mathcal{N} \left(\begin{bmatrix} 1 \\ 0 \end{bmatrix}, \frac{J}{2} \mathbf{I} \right), \quad f_{X, Y}(x, y) = \frac{1}{\pi J} \exp \left(-\frac{(x-1)^2 + y^2}{J} \right) \quad (3.38)$$

Transform to polar coordinates $x = \varrho \cos \phi$, $y = \varrho \sin \phi$ with Jacobian ϱ , giving

$$f_{R, \Phi}(\varrho, \phi) = \frac{\varrho}{\pi J} \exp \left(-\frac{(\varrho \cos \phi - 1)^2 + (\varrho \sin \phi)^2}{J} \right) = \frac{\varrho}{\pi J} \exp \left(-\frac{\varrho^2 - 2\varrho \cos \phi + 1}{J} \right), \quad (3.39)$$

for $\varrho \geq 0$ and $\phi \in [-\pi, \pi]$.

Integrating (3.39) over ϱ yields the phase density

$$\begin{aligned} p_\Phi(\phi) &= \int_0^\infty f_{R, \Phi}(\varrho, \phi) d\varrho \\ &= \frac{e^{-1/J}}{\pi J} \int_0^\infty \varrho \exp \left(-\frac{\varrho^2 - 2\varrho \cos \phi + 1}{J} \right) d\varrho. \end{aligned} \quad (3.40)$$

Complete the square: $\varrho^2 - 2\varrho \cos \phi = (\varrho - \cos \phi)^2 - \cos^2 \phi$. Then

$$p_\Phi(\phi) = \frac{e^{-1/J}}{\pi J} \exp\left(\frac{\cos^2 \phi}{J}\right) \int_0^\infty \varrho \exp\left(-\frac{(\varrho - \cos \phi)^2}{J}\right) d\varrho. \quad (3.41)$$

With the change of variables $u = (\varrho - \cos \phi)/\sqrt{J}$, so $\varrho = \sqrt{J}u + \cos \phi$ and $d\varrho = \sqrt{J}du$,

$$\begin{aligned} \int_0^\infty \varrho \exp\left(-\frac{(\varrho - \cos \phi)^2}{J}\right) d\varrho &= \sqrt{J} \int_{-\cos \phi/\sqrt{J}}^\infty (\sqrt{J}u + \cos \phi) e^{-u^2} du \\ &= \frac{J}{2} \exp\left(-\frac{\cos^2 \phi}{J}\right) + \cos \phi \sqrt{J} \int_{-\cos \phi/\sqrt{J}}^\infty e^{-u^2} du. \end{aligned} \quad (3.42)$$

Using $\int_a^\infty e^{-u^2} du = \frac{\sqrt{\pi}}{2} \operatorname{erfc}(a)$ and substituting into (3.41) gives the closed form

$$p_\Phi(\phi) = \frac{e^{-1/J}}{2\pi} \left[1 + \sqrt{\frac{\pi}{J}} \cos \phi \exp\left(\frac{\cos^2 \phi}{J}\right) \operatorname{erfc}\left(-\frac{\cos \phi}{\sqrt{J}}\right) \right], \quad \phi \in [-\pi, \pi]. \quad (3.43)$$

An equivalent numerically stable form follows from $\cos^2 \phi = 1 - \sin^2 \phi$.

$$p_\Phi(\phi) = \frac{1}{2\pi} \left[e^{-1/J} + \sqrt{\frac{\pi}{J}} \cos \phi \exp\left(-\frac{\sin^2 \phi}{J}\right) \operatorname{erfc}\left(-\frac{\cos \phi}{\sqrt{J}}\right) \right] \quad (3.44)$$

Since the model (3.37) is symmetric about $\phi = 0$, $\mathbb{E}[\Phi] = 0$ and

$$\sigma_\Phi^2 = \mathbb{E}[\Phi^2] = \int_{-\pi}^\pi \phi^2 p_\Phi(\phi) d\phi, \quad \sigma_\Phi = \sqrt{\sigma_\Phi^2}. \quad (3.45)$$

This one-dimensional integral can be evaluated numerically for any J .

For $J \ll 1$, the phase error concentrates near $\phi = 0$ and one recovers the usual small-error approximation

$$\sigma_\Phi^2(J) \approx \frac{J}{2}, \quad (3.46)$$

which matches the linearised relation $\Phi \approx \operatorname{Im} \varepsilon$ under (3.37). For $J \rightarrow \infty$, $Z_{\text{cal}} \approx \varepsilon$ is dominated by noise. $p_\Phi(\phi) \rightarrow \frac{1}{2\pi}$ and $\sigma_\Phi^2 \rightarrow \pi^2/3$ which is the maximum variance and no information is present.

3.4 Calibration Procedure

Ideally, calibration is performed on a stable oscillation. Algorithm 2 outlines the procedure. If the target frequency changes, C may need to be recomputed. For a fixed choice of window length N , sampling rate F_s , bandpass parameters

Table 1: Comparison of analytical and Monte Carlo phase standard deviations as a function of SNR_{in} . Monte Carlo values are reported over 10^5 trials.

SNR_{in}	Phase standard deviation $\sigma_\varphi [\circ]$		
	Monte Carlo	(3.34)	(3.45)
0.1	47.59	38.67	47.86
1	12.50	12.23	12.54
10	3.86	3.87	3.88
100	1.22	1.22	1.22

Algorithm 2 Abstract calibration procedure of the ecHT (with optional f_0 estimation)

Input: Window length N , sampling rate F_s , centre frequency f_0 , bandpass $(l_{\text{freq}}, h_{\text{freq}})$, filter order, FFT length L , data window $x[0:N - 1]$ (for f_0 estimation).

Output: Global calibration gain C_{opt}

- 1: **if** f_0 is unstable **then**
- 2: Estimate f_0 using a suitable spectral estimator
- 3: **end if**
- 4: Design f_0 -centred bandpass H
- 5: Compute G_\pm from (2.18), (2.19)
- 6: Compute MSE-optimal calibration gain

$$C_{\text{opt}} \leftarrow \frac{G_+^*}{|G_+|^2 + |G_-|^2}, \quad (3.47)$$

and residual error

$$J_{\text{opt}} \leftarrow \frac{|G_-|^2}{|G_+|^2 + |G_-|^2}. \quad (3.48)$$

- 7: Apply C_{opt} as a global complex multiplier to the ecHT output \hat{z}

$$\hat{z}_C \leftarrow C_{\text{opt}} \hat{z} \quad (3.49)$$

$(l_{\text{freq}}, h_{\text{freq}})$ and centre frequency f_0 , the ecHT endpoint error for a finite-length cosine can be written as

$$F(\varphi_0) = G_+ + G_- e^{-2j\varphi_0}, \quad (3.50)$$

where φ_0 is the (unknown) initial phase and $G_{+,-} \in \mathbb{C}$ are the phase-independent complex gains of the positive and negative frequency components induced by

ecHT. The MSE-optimal global scalar C_{opt} is obtained in Theorem 3

$$C_{\text{opt}} = \frac{\mathbb{E}[F^*]}{\mathbb{E}[|F|^2]} = \frac{G_+^*}{|G_+|^2 + |G_-|^2} \approx \frac{1}{G_+}, \quad (3.51)$$

and the corresponding minimal residual error is

$$J(C_{\text{opt}}) = \frac{|G_-|^2}{|G_+|^2 + |G_-|^2}. \quad (3.52)$$

Thus, the entire calibration is determined by these two complex numbers. G_+ describes the desired, phase-aligned response at f_0 and G_- quantifies the negative-frequency leakage that cannot be removed by a single scalar. The complexity of the calibration $\mathcal{O}(L)$ is negligible compared to the ecHT's complexity of $\mathcal{O}(L \log L)$. A python class implementing c-ecHT based on the python library `meegkit` [26] is available in Section 7.

4 Experiments

To summarise the phase-error distribution between the causal ecHT estimate $\hat{\theta}$ and an offline narrow-band reference θ , standard phase-synchrony statistics on the wrapped phase difference $\Delta\theta = \text{wrap}(\hat{\theta} - \theta)$ are used. The phase-locking value (PLV)

$$\text{PLV} = |\mathbb{E}[e^{j\Delta\theta}]|, \quad (4.1)$$

measures the concentration of $\Delta\theta$ on the unit circle (PLV $\rightarrow 1$ for a fixed phase relation; PLV $\rightarrow 0$ for broadly dispersed errors) [27].

The phase-lag index (PLI) captures the directional asymmetry of the phase-difference distribution [28]. Here, $\Delta\theta > 0$ indicates that the estimate $\hat{\theta}$ leads the reference and $\Delta\theta < 0$ indicates lag; thus PLI ≈ 0 implies a symmetric error distribution, whereas larger PLI imply errors of one sign, independent of the error concentration captured by PLV.

$$\text{PLI} = |\mathbb{E}[\text{sign}(\Delta\theta)]| \quad (4.2)$$

Table 2: Phase and amplitude error statistics before and after calibration.

Error	Phase [°]			Amplitude [%]		
	Mean	Std.Dev.	Max	Mean	Std.Dev.	Max
ecHT	8.81	1.87	11.67	3.73	2.44	7.69
c-ecHT	0.42	0.34	1.16	0.66	0.52	1.86

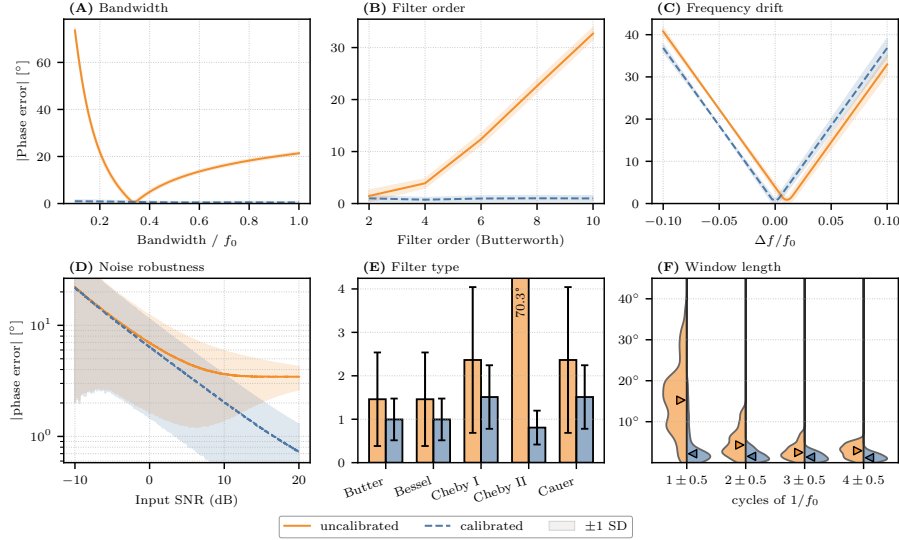


Figure 2: Parameter dependence of the ecHT endpoint phase error and effect of scalar calibration in single-tone simulations. Absolute endpoint phase error (deg) is shown for ecHT (orange) and c-ecHT (blue), with solid lines giving the mean and shaded bands indicating ± 1 SD. If not noted differently: $f_0 = 10$ Hz, $F_s = 256$ Hz, $N = \text{round}(2.1F_s/f_0)$, BW = $[0.7f_0, 1.3f_0]$, filter order 2. Window length is chosen slightly imperfectly to simulate realistic conditions. Across all panels, the analytic single-tone calibration reduces systematic phase bias while preserving the variability predicted by the complex-gain and leakage analysis. **(A)** Dependence on relative filter bandwidth (bandwidth/ f_0). **(B)** Filter order. **(C)** Frequency detuning $\Delta f / f_0$. **(D)** Input SNR (log₁₀ y -axis). **(E)** Comparison of IIR filter families (Butterworth, Bessel, Chebyshev I & II, Cauer/elliptic; bars show mean, error bars SD). **(F)** Distribution of absolute endpoint error for non-integer window lengths spanning 1-4 cycles around f_0 (half-violins for uncalibrated vs calibrated, markers denote medians).

4.1 Simulation

In their original publication, Schreglmann et al. [3] swept a tone from 2 to 3 Hz at $F_s = 256$ Hz with a window length $N = 256$. The bandpass filter had a bandwidth of 1.5 Hz and centred around 3 Hz. The reference phase is defined as the offline phase of the analytic signal [29]. Their reported number can be verified and improved by calibration substantially as seen in Tab. 2. The residual error arises from the fact that the calibration reduces the average error across all initial phases. Here, an error of 8.81° would result in a timing offset of up to 12 ms.

As an additional experiment, a tone $f_0 = 10$ Hz was iterated across a wide range of parameters represented in Fig. 2. Across all experiments, c-ecHT outperforms ecHT. Further, Fig. 2 shows how the ecHT is a parameter-dependent

algorithm and becomes through calibration virtually independent of parameter choice. Therefore, any free parameters can be chosen to fit a specific application (e.g. window length according to frequency stability or computational budget, and filter parameters according to noise estimates or frequency stability). The presented ecHT results are similar to [3], [4], [11].

Computational cost was evaluated on two processors in Tab. 3. Compared to a standard FFT-based Hilbert transform with the same length, the ecHT produced only a modest overhead ($\sim 1.1 \dots 1.8 \times$, median $\sim 1.4 \times$), reflecting the additional bandpass and calibration operations while remaining well within real-time constraints.

Table 3: Computational cost of block-wise ecHT.

CPU		
	i7-14700KF	i5-1335U
<i>Runtime</i> [μs]		
$N = 256$	17.0	38.9
$N = 1024$	24.8	49.4
$N = 16\,384$	204.1	389.1
<i>Amortised cost</i> [ns/sample]		
Min	12.7	24.3
Median	16.7	33.3
Max	66.4	140.1
Overhead vs. HT [\times]	1.4 (median)	

In line with our results, Liufu et al. found that the ecHT yielded higher phase accuracy and consistency than a standard Hilbert approach on EEG, local field potential, and tremor signals [11].

4.2 EEG Alpha Phase

Data recorded from the sleep staging database of the Haaglanden Medisch Centrum (HMC) consisting of 150 nights from a heterogeneous population was chosen [30], [31], [32]. EEG data was extracted from Wake until the first change in sleep stage. The individual alpha frequency (IAF) was estimated from O2-M1 using a Savitzky-Golay filter [33]. Ground truth phase estimations were acquired using an offline Hilbert transform applied to acausally filtered data (bandwidth: $[0.7f_0, 1.3f_0]$, filter order 2). In the 110 recordings where an IAF was detectable, c-ecHT performed significantly ($p < 10^{-6}$) better than ecHT (Fig. 3). The ecHT error is comparable to that reported in the literature [4], [7].

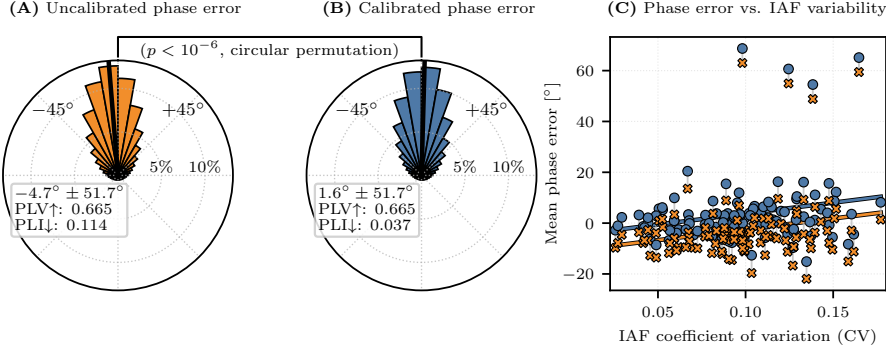


Figure 3: Causal alpha-phase estimation with the ecHT on the HMC sleep EEG dataset. $F_s = 256$ Hz, $N = 2F_s/f_0$, $\text{BW} = [0.7f_0, 1.3f_0]$, filter order 2 **(A)** ecHT shows a systematic phase bias and elevated PLI in the distribution of alpha-band phase errors across all samples. **(B)** Applying the analytic calibration removes the bulk of this bias, preserves phase locking (PLV), and substantially reduces PLI. **(C)** Across recordings, the c-ecHT attenuates the dependence of mean phase error on individual alpha-frequency variability, indicating improved robustness to spectral instability.

The mean phase error reduced from -4.7° to 1.6° , which also reduced PLI. The variance and PLV remain unchanged, since they cannot be changed by a scalar calibration. These results are consistent with previous findings [4], [12]. Additionally, Fig. 3C shows the error with respect to the coefficient of variance (standard deviation normalised by the mean). It is apparent that an unstable IAF leads to a greater phase error. Calibration also improves this dependency. IAF should be estimated regularly to correct the parameters of the ecHT algorithm. If online centre frequency tracking is not feasible, the variance can be estimated and the calibration factor adjusted empirically.

Inference was performed at the recording level for the calibration effect on mean phase error to avoid pseudoreplication. We used a paired label-swap permutation test (a within-recording swap of uncalibrated vs. calibrated labels), with test statistic

$$\left| \text{wrap} \left(\arg \left\{ \sum_i w_i e^{j\mu_i^{\text{unc}}} \right\} - \arg \left\{ \sum_i w_i e^{j\mu_i^{\text{cal}}} \right\} \right) \right| \quad (4.3)$$

where μ_i are per-recording circular mean errors and w_i are per-recording sample counts. The permutation count was 100 000. The analysis shows that calibration induces a robust and highly consistent reduction in phase bias, behaving like a near-deterministic bias correction. At the recording level ($N = 110$), calibration shifted the circular mean phase error by -6.28° (95% bootstrap CI $[-6.50^\circ, -6.02^\circ]$). A paired label-swap permutation test (100 000 permutations) confirmed this effect was highly significant ($p < 10^{-6}$). The magnitude of the correction was consistent across recordings (MAD = 6.28° , 95% CI $[6.02^\circ, 6.50^\circ]$).

$6.50^\circ]$), yielding an extremely large standardised paired effect ($d_n = -6.94$, 95% CI $[-7.83, -6.36]$).

A paired circular permutation test was used to assess differences in mean phase error between uncalibrated and calibrated conditions. For each recording, circular mean phase angles were computed, and labels were randomly swapped within pairs, preserving within-recording dependence, to generate a null distribution of absolute mean-direction differences. The two-sided p -value was obtained as the proportion of permutations in which the permuted statistic exceeded the observed circular mean difference.

4.3 Tremor Phase

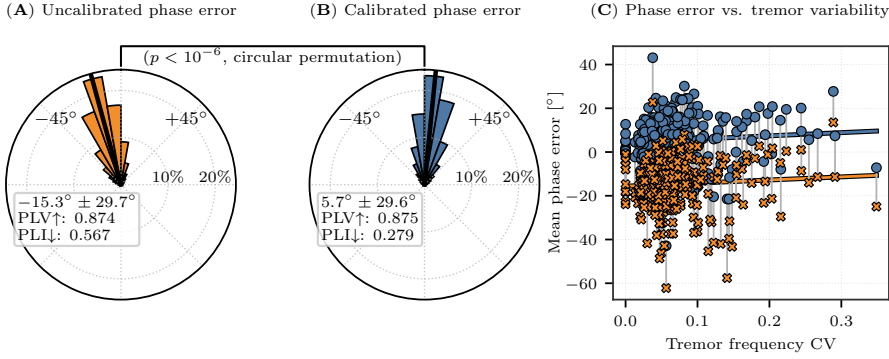


Figure 4: **Causal phase estimation with the ecHT on tremor data.** BW = $[0.5f_0, 1.5f_0]$, $F_s \approx 500$ Hz, $N = 128$, filter order 4. **(A)** ecHT shows a systematic phase bias and elevated PLI in the distribution of phase errors across all samples. **(B)** Applying the analytic calibration removes the bulk of this bias, preserves phase locking (PLV), and substantially reduces PLI. **(C)** Across recordings, the c-ecHT attenuates the dependence of mean phase error on frequency variability, indicating improved robustness to spectral instability.

Schreglmann et al. [3] investigated how essential tremor (ET) can be reduced by phase-locked transcranial electrical stimulation. Tremor signals are lower in frequency compared to the alpha band. In their experiments, the phase of the ET was calculated using the ecHT and then stimulated at pre-defined phases. The authors provide their recordings [34]. We carried out our phase estimations with the original parameters (filter bandwidth: $[0.5f_0, 1.5f_0]$, filter order: 4, window length: 128 samples). The calibration results in Fig. 4 show a statistically significant ($p < 10^{-6}$) improvement in mean phase error from -15.3° to 5.7° .

Most of the residual error after calibration stems from a change in f_0 . For this reason, f_0 can be tracked, and the calibration can be carried using the most recent f_0 estimate. We re-estimated f_0 (approximately every 4 s) from the

tremor signal using a simple spectral peak estimate, and then re-centred the bandpass and re-computed the analytic calibration for the updated f_0 . This isolates the residual error attributable to leakage/noise from the bias caused by centre-frequency drift, reducing the mean error to 0.1° and slightly lowering the standard deviation, as depicted in Fig. 5. For this application the system can be considered fully calibrated.

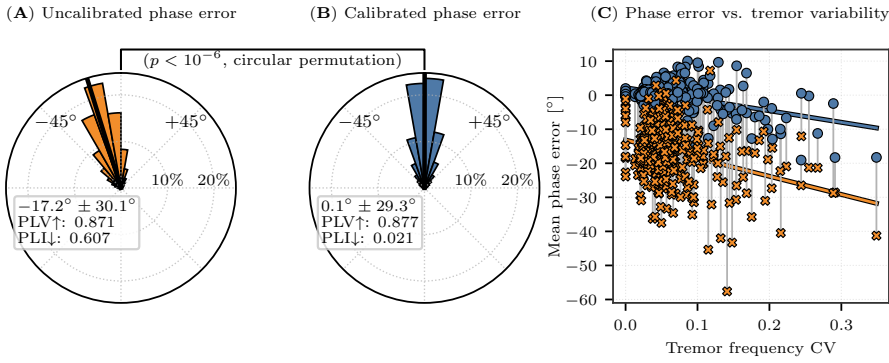


Figure 5: **Causal tremor-phase estimation with the ecHT on the replication tremor data with centre-frequency tracking.** (A) With centre-frequency tracking but without calibration, ecHT shows a slightly higher systematic phase bias and elevated PLI. (B) With analytic calibration and periodic f_0 updates, mean phase bias is reduced to 0.1° while PLV is preserved and PLI is strongly reduced. (C) Mean phase error versus tremor frequency variability, showing improved robustness under drift.

However, tracking the centre frequency makes the ecHT endpoint bias time-varying. Without calibration this bias is no longer constant, thereby increasing phase error. In contrast, c-ecHT explicitly compensates for the frequency-dependent bias at each tracked frequency.

5 Practical Considerations

As Liufu et al. [11] and Zrenner et al. [29] also observed, different parameter settings result in different errors, and a compromise usually needs to be made between a constant phase bias, which is determined by the phase response (group delay) of the bandpass filter, and cycle-to-cycle ripple/variance, which is caused by finite-window spectral leakage (including negative-frequency leakage). Global calibration can remove most static bias, but cannot eliminate the variance floor induced by leakage, noise and frequency drift.

5.1 Window Length

Increasing the window length N reduces leakage (i.e. smaller ripple/variance) as well as DFT resolution $\Delta f = F_s/N$, thereby improving alignment between f_0 and its nearest bin. In practice, the cleanest endpoint behaviour is achieved when the window spans approximately an integer number of cycles.

$$N \frac{f_0}{F_s} - \text{round} \left(N \frac{f_0}{F_s} \right) \approx 0, \quad (5.1)$$

However, longer windows assume that the oscillation is stationary throughout; if the frequency drifts, the error increases. For non-stationary rhythms, Liufu et al. report the best performance around one-cycle windows [11], whereas we noted best performance with two-cycle windows. Also, avoid tapered windows (e.g. Hann) for online endpoint use, as they down-weight the newest samples.

Recommendation Use low-integer-cycle windows when the frequency is variable; otherwise use longer, near-integer-cycle windows to reduce leakage.

5.2 Filter Bandwidth

A low bandwidth is used to suppress off-target frequency components. However, bandwidth can be seen as a *robustness knob*: narrower is not always better. Narrowing the passband increases group delay, which manifests as a constant phase offset. This offset can be calibrated if f_0 is stable, but it also makes the estimate more sensitive to detuning/drift, with phase error growing roughly according to

$$\varepsilon_\theta \approx -\Delta\omega\tau_g(\omega_0). \quad (5.2)$$

Recommendation Use the narrowest possible bandwidth that still covers the expected f_0 -variability. If the true frequency is uncertain or drifting, use a slightly wider filter and/or actively track f_0 , updating the filter and calibration as necessary.

5.3 Filter Order

Higher-order filters generally increase group delay, thereby steepening the local phase slope around ω_0 . Consequently, even a small centre-frequency mismatch produces a phase error (Fig. 2C). High order can also make the passband phase less locally linear, reducing predictability.

Recommendation Use minimal-order filters (2) and avoid increasing the order unless you can tolerate extra delay/bias and increased sensitivity to detuning.

5.4 Centre Frequency Estimate

The performance of the ecHT depends critically on centring the filter at the true oscillation frequency. Any mismatch samples the filter's phase response at the

incorrect point, resulting in a phase error proportional to the group delay. This is an unavoidable limitation of causal filtering: even after calibration removes the offset at the nominal f_0 , frequency drift creates a time-varying bias. For non-stationary oscillations, track f_0 and update the filter centre frequency and calibration as needed [33].

Recommendation Continuously re-estimate/track f_0 in non-stationary settings; treat calibration as frequency-specific, refreshing it when f_0 changes.

5.5 Sampling Rate, Zero-Padding & Filter Type

These choices are secondary, but still important for numerical fidelity. Higher sampling rates generally improve the spectral representation. Zero-padding increases the density of DFT bins, which can help to evaluate H closer to the true f_0 , but it does not change the fundamental leakage-delay trade-off. Finally, Liufu et al. as well as Fig. 2E display little difference across common IIR families (e.g. Butterworth, Chebyshev, Cauer) for the ecHT performance [11]; as their differences become more prominent at higher filter orders, Butterworth is a reasonable default.

Recommendation Use zero-padding only for finer frequency grid evaluation. Prefer a sufficient F_s and default to Butterworth unless you have a specific reason not to.

5.6 DFT Grid

Evaluate the filter response exactly at the FFT/DFT bin frequencies used by the transform. Avoid rounding bin frequencies (by using $\lceil f_k \rceil$): this creates a frequency-grid mismatch that manifests as an avoidable phase bias. In typical settings, removing this rounding substantially reduces the ecHT mean phase error, especially if the window length is not an integer multiple of the sampling rate or the sampling rate varies.

6 Discussion

Reliable phase estimates are essential for closed-loop (brain) stimulation, yet causal filtering and finite-window Hilbert methods are particularly susceptible to errors in this context. The estimator must extrapolate the analytic signal to the boundary of the observation window, where spectral leakage and filter phase distortions are maximal. In this study, we analytically characterise the boundary effects of the endpoint-corrected Hilbert transform and demonstrate that a simple calibration produces a statistically robust estimator with consistent performance and clear design rules.

Notably, the ecHT endpoint for a narrow-band oscillation can be decomposed into two contributions: a desired positive-frequency term G_+ and a negative-frequency leakage term G_- , which turn filter and window choice into interpretable quantities. This decomposition separates the ecHT errors into a nearly constant phase bias driven by the filter's phase response and a phase-dependent wobble that varies with the unknown phase and cannot be eliminated by a fixed time shift.

This view distinguishes between what is correctable and intrinsic errors. When negative-frequency leakage is small, the ecHT behaves approximately like the true analytic endpoint, scaled by a complex factor. As leakage increases, the estimator becomes a mixture, whose phase depends on the (unknown) phase itself. The deterministic bounds derived in the single-tone setting illustrate this: the phase deviation from the positive-frequency component is uniformly bounded by $\arcsin |G_-|/|G_+|$. In practice, this means that suppressing leakage is not merely *nice to have*; it is essential for keeping the worst-case phase errors small.

6.1 Optimal Calibration

The scalar calibration factor introduced in Sec. 3 is the mean-square optimal linear map from the ecHT endpoint \hat{Z} to the ideal analytic endpoint Z . Geometrically, it is the orthogonal projection of Z onto the subspace spanned by \hat{Z} and is statistically equivalent to a Wiener estimator. This has two immediate consequences.

Firstly, calibration targets the systematic gain encoded by G_+ . This removes the constant phase bias and amplitude scaling when the correlation between \hat{Z} and Z remains high. Empirically, this is reflected in a substantial reduction in phase errors: systematic phase bias is removed while preserving phase locking and reducing asymmetry. These improvements are significant: a phase bias of only a few degrees can result in timing offset of several milliseconds, which could be substantial relative to the stimulation window.

Secondly, the Wiener interpretation makes the irreducible error floor explicit. Calibration can only recover information that is present in \hat{Z} . This explains why calibration reduces mean bias more than variability: it fixes the coherent error but not the incoherent component induced by leakage and non-stationarity. In other words, the c-ecHT provides unbiased endpoint phase estimates under stable conditions, while any remaining jitter reflects either intrinsic limitations of the estimator or genuine instability of the signal.

Stable conditions can be approximated by tracking f_0 . When the calibration is at the (updated) centre frequency, the remaining systematic bias collapses to practically zero, implying that most of the residual mean error in Sec. 4.2 and 4.3 was drift-induced rather than a failure of the calibration.

6.2 Implications for Closed-Loop Use

Phase estimators should be evaluated by both their absolute error and the structure of their residuals. Does the ecHT primarily introduce a constant phase offset or phase-dependent distortions? The bias-variance decomposition (Sec. 3.1) shows that the ecHT can introduce a systematic bias, meaning that estimator artefacts may appear as physiological phase asymmetries. Calibration substantially reduces this, while maintaining PLV, thereby improving the interpretability of downstream statistics.

The ecHT remains computationally efficient as it is FFT-based with $\mathcal{O}(L \log L)$ complexity. The additional endpoint correction and calibration produce only modest overhead. This keeps the method compatible with embedded or real-time pipelines, where latency budgets are tight. The calibration can be used as a drop-in improvement for existing ecHT pipelines using the provided script in Sec. 7.

6.3 Limitations

The calibration factor is frequency-specific because both G_+ and G_- both depend on the way in which the filter samples the spectrum around the assumed centre frequency f_0 . If f_0 drifts, the phase bias becomes time-varying, which can introduce bias if the calibration is fixed. This motivates adaptive frequency tracking and periodic recalibration.

The single-tone derivation assumes stationarity over the analysis window. Transient bursts, artefacts, and within-window changes violate this assumption and can amplify leakage. Robust estimation or explicit artefact rejection is a necessary companion for real-world deployment. Also, phase may be poorly defined during low-amplitude windows.

When multiple nearby frequency components coexist nearby, a single centre frequency does not fully describe the signal. In such settings, the scalar calibration remains the MSE-optimal correction for the reference definition of Z , but its meaning depends on how the reference signal is constructed. More importantly, true phase can become model-dependent. Performance claims should be interpreted as agreement with a specified reference pipeline, not an absolute ground truth.

6.4 Outlook

The theoretical characterisation here suggests several concrete extensions that could make the c-ecHT a more general algorithm for real-time (neural) signal processing.

Optimal calibration is defined not only for the single-tone case, but also for general complex random variables (Z, \hat{Z}). This enables the ecHT to be calibrated against a reference constructed from real data, providing an opportunity to learn the most effective correction for the actual environment. The empirical estimator's asymptotic properties provide a basis for estimating uncertainty in calibration and for deciding when recalibration is statistically warranted.

Applications may require the simultaneous tracking of multiple rhythms or the distinction of narrow-band oscillations. A c-ecHT filter bank using one analytic mask per band and a band-specific calibration, would allow phase estimation across frequencies, while making inter-band interference and leakage measurable.

Finally, a multivariate generalisation would replace the scalar coefficient with a matrix that maps a vector of ecHT endpoints (across channels or spatially filtered components) onto a reference vector. This could unify endpoint correction with spatial filtering, which would have a significant impact on EEG/MEG and multi-contact invasive recordings in particular.

6.5 Conclusion

These results establish the c-ecHT as an intermediate solution between simple causal filters and more complex adaptive models. By decomposing endpoint distortion into a correctable gain term and an irreducible leakage term, the current framework offers both a practical tool and a diagnostic language to explain when and why phase estimation fails. The combination of theoretical transparency, computational efficiency and a clear path to future extensions makes the ecHT a strong candidate for standardised real-time phase estimation, provided that its requirements regarding frequency stability and artefact robustness are addressed.

7 Code availability

Code for the performed experiments is available from GitHub at <https://github.com/eosmers/cecHT>

8 Author Contributions

E.O. and D.K. wrote the manuscript. E.O. performed the mathematical calculations, E.O. designed and performed all data analyses, D.K. supervised the study.

9 Competing Interests

The authors declare no competing interests.

References

- [1] J. Gross, “Analytical methods and experimental approaches for electrophysiological studies of brain oscillations,” *Journal of Neuroscience Methods*, vol. 228, pp. 57–66, May 2014, ISSN: 01650270. DOI: [10.1016/j.jneumeth.2014.03.007](https://doi.org/10.1016/j.jneumeth.2014.03.007) Accessed: 10th Dec. 2025.
- [2] C. Zrenner and U. Ziemann, “Closed-Loop Brain Stimulation,” *Biological Psychiatry*, vol. 95, no. 6, pp. 545–552, Mar. 2024, ISSN: 00063223. DOI: [10.1016/j.biopsych.2023.09.014](https://doi.org/10.1016/j.biopsych.2023.09.014) Accessed: 10th Feb. 2025.
- [3] S. R. Schreglmann et al., “Non-invasive suppression of essential tremor via phase-locked disruption of its temporal coherence,” *Nature Communications*, vol. 12, no. 1, p. 363, Jan. 2021, ISSN: 2041-1723. DOI: [10.1038/s41467-020-20581-7](https://doi.org/10.1038/s41467-020-20581-7) Accessed: 18th Jul. 2024.
- [4] S. Bressler, R. Neely, R. M. Yost, D. Wang and H. L. Read, “A wearable EEG system for closed-loop neuromodulation of sleep-related oscillations,” *Journal of Neural Engineering*, vol. 20, no. 5, p. 056030, Oct. 2023, ISSN: 1741-2560, 1741-2552. DOI: [10.1088/1741-2552/acfb3b](https://doi.org/10.1088/1741-2552/acfb3b) Accessed: 12th Jul. 2024.
- [5] S. Bressler, R. Neely, R. M. Yost and D. Wang, “A randomized controlled trial of alpha phase-locked auditory stimulation to treat symptoms of sleep onset insomnia,” *Scientific Reports*, vol. 14, no. 1, p. 13039, Jun. 2024, ISSN: 2045-2322. DOI: [10.1038/s41598-024-63385-1](https://doi.org/10.1038/s41598-024-63385-1) Accessed: 11th Jul. 2024.
- [6] T. J. Harlow, S. M. Marquez, S. Bressler and H. L. Read, “Individualized Closed-Loop Acoustic Stimulation Suggests an Alpha Phase Dependence of Sound Evoked and Induced Brain Activity Measured with EEG Recordings,” *eNeuro*, vol. 11, no. 6, ENEURO.0511-23.2024, Jun. 2024, ISSN: 2373-2822. DOI: [10.1523/ENEURO.0511-23.2024](https://doi.org/10.1523/ENEURO.0511-23.2024) Accessed: 6th Nov. 2025.
- [7] H. Hebron et al., “A closed-loop auditory stimulation approach selectively modulates alpha oscillations and sleep onset dynamics in humans,” *PLOS Biology*, vol. 22, no. 6, S. Hanslmayr, Ed., e3002651, Jun. 2024, ISSN: 1545-7885. DOI: [10.1371/journal.pbio.3002651](https://doi.org/10.1371/journal.pbio.3002651) Accessed: 20th Mar. 2025.
- [8] V. Jaramillo et al., “Closed-loop auditory stimulation targeting alpha and theta oscillations during rapid eye movement sleep induces phase-dependent power and frequency changes,” *SLEEP*, vol. 47, no. 12, zsa193, Dec. 2024, ISSN: 0161-8105, 1550-9109. DOI: [10.1093/sleep/zsa193](https://doi.org/10.1093/sleep/zsa193) Accessed: 6th Nov. 2025.

- [9] M. Vinao-Carl et al., “Just a phase? Causal probing reveals spurious phasic dependence of sustained attention,” *NeuroImage*, vol. 285, p. 120 477, Jan. 2024, ISSN: 10538119. DOI: 10.1016/j.neuroimage.2023.120477 Accessed: 19th Mar. 2025.
- [10] J. L. Busch, L. K. Feldmann, A. A. Kühn and M. Rosenblum, “Real-time phase and amplitude estimation of neurophysiological signals exploiting a non-resonant oscillator,” *Experimental Neurology*, vol. 347, p. 113 869, Jan. 2022, ISSN: 00144886. DOI: 10.1016/j.expneurol.2021.113869 Accessed: 24th Sep. 2024.
- [11] M. Liufu, Z. M. Leveroni, S. Shridhar, N. Zhou and J. Y. Yu, “Optimizing real-time phase detection in diverse rhythmic biological signals for phase-specific neurostimulation,” *Journal of Neural Engineering*, vol. 22, no. 5, p. 056 037, Oct. 2025, ISSN: 1741-2560, 1741-2552. DOI: 10.1088/1741-2552/ae10e1 Accessed: 26th Nov. 2025.
- [12] C. Zrenner, D. Desideri, P. Belardinelli and U. Ziemann, “Real-time EEG-defined excitability states determine efficacy of TMS-induced plasticity in human motor cortex,” *Brain Stimulation*, vol. 11, no. 2, pp. 374–389, Mar. 2018, ISSN: 1935861X. DOI: 10.1016/j.brs.2017.11.016 Accessed: 18th Jul. 2024.
- [13] S. Shirinpour, I. Alekseichuk, K. Mantell and A. Opitz, “Experimental evaluation of methods for real-time EEG phase-specific transcranial magnetic stimulation,” *Journal of Neural Engineering*, vol. 17, no. 4, p. 046 002, Jul. 2020, ISSN: 1741-2552. DOI: 10.1088/1741-2552/ab9dba Accessed: 18th Jul. 2024.
- [14] B. Kim et al., “EEG Phase Can Be Predicted with Similar Accuracy across Cognitive States after Accounting for Power and Signal-to-Noise Ratio,” *eNeuro*, vol. 10, no. 9, ENEURO.0050-23.2023, Sep. 2023, ISSN: 2373-2822. DOI: 10.1523/ENEURO.0050-23.2023 Accessed: 9th Dec. 2025.
- [15] K. H. Madsen, A. N. Karabanov, L. G. Krohne, M. G. Safeldt, L. Tomasevic and H. R. Siebner, “No trace of phase: Corticomotor excitability is not tuned by phase of pericentral mu-rhythm,” *Brain Stimulation*, vol. 12, no. 5, pp. 1261–1270, Sep. 2019, ISSN: 1935861X. DOI: 10.1016/j.brs.2019.05.005 Accessed: 9th Dec. 2025.
- [16] T. Onojima and K. Kitajo, “A state-informed stimulation approach with real-time estimation of the instantaneous phase of neural oscillations by a Kalman filter,” *Journal of Neural Engineering*, vol. 18, no. 6, p. 066 001, Dec. 2021, ISSN: 1741-2560, 1741-2552. DOI: 10.1088/1741-2552/ac2f7b Accessed: 10th Dec. 2025.
- [17] A. Wodeyar, M. Schatza, A. S. Widge, U. T. Eden and M. A. Kramer, “A state space modeling approach to real-time phase estimation,” *eLife*, vol. 10, e68803, Sep. 2021, ISSN: 2050-084X. DOI: 10.7554/eLife.68803 Accessed: 10th Dec. 2025.

- [18] A. Wodeyar, F. A. Marshall, C. J. Chu, U. T. Eden and M. A. Kramer, “Different Methods to Estimate the Phase of Neural Rhythms Agree But Only During Times of Low Uncertainty,” *eNeuro*, vol. 10, no. 11, EN-EURO.0507–22.2023, Nov. 2023, ISSN: 2373-2822. DOI: 10.1523/ENEURO.0507–22.2023 Accessed: 10th Dec. 2025.
- [19] M. Makarova, N. Fedosov, J. Nekrasova and A. Ossadtchi, “Hardware-enabled low latency rhythmic brain state tracking for brain stimulation applications,” *NeuroImage*, vol. 319, p. 121437, Oct. 2025, ISSN: 10538119. DOI: 10.1016/j.neuroimage.2025.121437 Accessed: 10th Dec. 2025.
- [20] G. Santostasi et al., “Phase-locked loop for precisely timed acoustic stimulation during sleep,” *Journal of Neuroscience Methods*, vol. 259, pp. 101–114, Feb. 2016, ISSN: 01650270. DOI: 10.1016/j.jneumeth.2015.11.007 Accessed: 5th Feb. 2025.
- [21] M. Rosenblum, A. Pikovsky, A. A. Kühn and J. L. Busch, “Real-time estimation of phase and amplitude with application to neural data,” *Scientific Reports*, vol. 11, no. 1, p. 18037, Sep. 2021, ISSN: 2045-2322. DOI: 10.1038/s41598-021-97560-5 Accessed: 24th Sep. 2024.
- [22] H. Cho et al., “Development and Evaluation of a Real-Time Phase-Triggered Stimulation Algorithm for the CorTec Brain Interchange,” *IEEE Transactions on Neural Systems and Rehabilitation Engineering*, vol. 32, pp. 3625–3635, 2024, ISSN: 1534-4320, 1558-0210. DOI: 10.1109/TNSRE.2024.3459801 Accessed: 10th Dec. 2025.
- [23] H. Liu et al., “A Novel Real-time Phase Prediction Network in EEG Rhythm,” *Neuroscience Bulletin*, vol. 41, no. 3, pp. 391–405, Mar. 2025, ISSN: 1673-7067, 1995-8218. DOI: 10.1007/s12264-024-01321-z Accessed: 10th Dec. 2025.
- [24] M. L. Ferster et al., “Benchmarking Real-Time Algorithms for In-Phase Auditory Stimulation of Low Amplitude Slow Waves With Wearable EEG Devices During Sleep,” *IEEE Transactions on Biomedical Engineering*, vol. 69, no. 9, pp. 2916–2925, Sep. 2022, ISSN: 0018-9294, 1558-2531. DOI: 10.1109/TBME.2022.3157468 Accessed: 19th Sep. 2024.
- [25] A. V. Oppenheim and R. W. Schafer, *Discrete-Time Signal Processing*, Third international edition. Noida (India): Pearson, Dorling Kindersley, 2014, ISBN: 978-93-325-3503-9.
- [26] N. Barascud et al., *Nbara/python-meegkit: V0.1.7*, Zenodo, Dec. 2023. DOI: 10.5281/ZENODO.10303516 Accessed: 4th Dec. 2025.
- [27] J.-P. Lachaux, E. Rodriguez, J. Martinerie and F. J. Varela, “Measuring phase synchrony in brain signals,” *Human Brain Mapping*, vol. 8, no. 4, pp. 194–208, 1999, ISSN: 1065-9471, 1097-0193. DOI: 10.1002/(sici)1097-0193(1999)8:4%3C194::aid-hbm4%3E3.0.co;2-c Accessed: 15th Oct. 2024.

[28] C. J. Stam, G. Nolte and A. Daffertshofer, “Phase lag index: Assessment of functional connectivity from multi channel EEG and MEG with diminished bias from common sources,” *Human Brain Mapping*, vol. 28, no. 11, pp. 1178–1193, Nov. 2007, ISSN: 1065-9471, 1097-0193. DOI: 10.1002/hbm.20346 Accessed: 15th Oct. 2024.

[29] C. Zrenner, D. Galevska, J. O. Nieminen, D. Baur, M.-I. Stefanou and U. Ziemann, “The shaky ground truth of real-time phase estimation,” *NeuroImage*, vol. 214, p. 116 761, Jul. 2020, ISSN: 10538119. DOI: 10.1016/j.neuroimage.2020.116761 Accessed: 28th Jan. 2025.

[30] D. Alvarez-Estevez and R. M. Rijsman, “Inter-database validation of a deep learning approach for automatic sleep scoring,” *PLOS ONE*, vol. 16, no. 8, Y. Qiu, Ed., e0256111, Aug. 2021, ISSN: 1932-6203. DOI: 10.1371/journal.pone.0256111 Accessed: 9th Jul. 2025.

[31] D. Alvarez-Estevez and R. Rijsman, *Haaglanden Medisch Centrum sleep staging database*. DOI: 10.13026/T79Q-FR32 Accessed: 9th Jul. 2025.

[32] A. L. Goldberger et al., “PhysioBank, PhysioToolkit, and PhysioNet: Components of a New Research Resource for Complex Physiologic Signals,” *Circulation*, vol. 101, no. 23, Jun. 2000, ISSN: 0009-7322, 1524-4539. DOI: 10.1161/01.CIR.101.23.e215 Accessed: 5th Feb. 2025.

[33] A. W. Corcoran, P. M. Alday, M. Schlesewsky and I. Bornkessel-Schlesewsky, “Toward a reliable, automated method of individual alpha frequency (IAF) quantification,” *Psychophysiology*, vol. 55, no. 7, e13064, Jul. 2018, ISSN: 0048-5772, 1469-8986. DOI: 10.1111/psyp.13064 Accessed: 2nd Dec. 2025.

[34] S. Schreglmann et al., *Replication Data for: Non-invasive Suppression of Essential Tremor via Phase-Locked Disruption of its Temporal Coherence*, 2020. DOI: 10.7910/DVN/Z6EN21 Accessed: 20th Jan. 2026.

[35] G. Casella and R. L. Berger, *Statistical Inference*, 2. ed. Pacific Grove, Calif: Duxbury, 2002, ISBN: 978-0-534-24312-8.

[36] S. Blanco, H. Garcia, R. Quiroga, L. Romanelli and O. Rosso, “Stationarity of the EEG series,” *IEEE Engineering in Medicine and Biology Magazine*, vol. 14, no. 4, pp. 395–399, Jul. 1995, ISSN: 07395175. DOI: 10.1109/51.395321 Accessed: 2nd Dec. 2025.

[37] G. Florian and G. Pfurtscheller, “Dynamic spectral analysis of event-related EEG data,” *Electroencephalography and Clinical Neurophysiology*, vol. 95, no. 5, pp. 393–396, Nov. 1995, ISSN: 00134694. DOI: 10.1016/0013-4694(95)00198-8 Accessed: 2nd Dec. 2025.

[38] A. A. Fingelkurts and A. A. Fingelkurts, “Editorial: EEG Phenomenology and Multiple Faces of Short-term EEG Spectral Pattern,” *The Open Neuroimaging Journal*, vol. 4, no. 1, pp. 111–113, Sep. 2010, ISSN: 1874-4400. DOI: 10.2174/1874440001004010111 Accessed: 2nd Dec. 2025.

[39] V. Lawhern, S. Kerick and K. A. Robbins, “Detecting alpha spindle events in EEG time series using adaptive autoregressive models,” *BMC Neuroscience*, vol. 14, no. 1, p. 101, Dec. 2013, ISSN: 1471-2202. DOI: 10.1186/1471-2202-14-101 Accessed: 2nd Dec. 2025.

A Notation

Table 4: Summary of notation.

n	time bins
k	frequency bins
$x(n)$	Discrete-time real-valued input signal
$X(k)$	DFT of the windowed signal
F_s	Sampling rate (Hz)
N	Window length (number of samples)
L	DFT/FFT length ($L \geq N$)
f_0	Centre frequency of the target oscillation (Hz)
ω_0	Centre angular frequency, $\omega_0 = 2\pi f_0 / F_s$
k	DFT bin index, $k = 0, \dots, L - 1$
f_k	Frequency of bin k , $f_k = kF_s / L$
ω_k	Angular frequency of bin k , $\omega_k = 2\pi k / L$
\mathcal{P}	Set of strictly positive-frequency DFT bins
$m(k)$	Analytic-signal mask in the frequency domain
$H(k)$	Discrete frequency response of the bandpass filter
$H_{\text{eff}}(k)$	Effective ecHT response, $H_{\text{eff}}(k) = m(k)H(k)$
$z(n)$	analytic signal
$\hat{z}(n)$	analytic signal estimate
\hat{z}_{end}	Endpoint analytic estimate, $\hat{z}(N - 1)$
$\theta(n)$	True instantaneous phase, $\arg z(n)$
$\hat{\theta}(n)$	Instantaneous phase estimate, $\arg \hat{z}(n)$
F	effective endpoint complex gain
G_+	effective gain on positive-frequency component (main-lobe gain)
G_-	effective gain on negative-frequency component (leakage gain)
C	Calibration factor

B Proofs & Derivations

B.1 Deterministic phase-ripple and amplitude bounds

Proof of Theorem 1. Fix $\varphi_0 \in \mathbb{R}$.

$$F(\varphi_0) = G_+ + G_- e^{-j2\varphi_0} = G_+ (1 + u(\varphi_0)), \quad u(\varphi_0) = \frac{G_-}{G_+} e^{-j2\varphi_0} \quad (\text{B.1})$$

Then $|u(\varphi_0)| = |G_-|/|G_+| = r \in [0, 1]$ and, with $\alpha = \arg G_+$,

$$\delta_\theta(\varphi_0) = \arg F(\varphi_0) - \alpha = \arg(1 + u(\varphi_0)). \quad (\text{B.2})$$

Phase-ripple bound. The goal is to bound $|\delta_\theta(\varphi_0)|$ uniformly in the unknown initial phase φ_0 . Since $\delta_\theta(\varphi_0)$ depends on φ_0 only through $u(\varphi_0)$, it suffices to characterise the set of all possible values of $\arg(1+u)$ under the constraint $|u|=r$.

Because $|u(\varphi_0)|=r$ is fixed while the phase of $u(\varphi_0)$ varies with φ_0 , we may write $u(\varphi_0)=r e^{j\psi}$ for some $\psi \in \mathbb{R}$. Hence

$$\delta_\theta(\varphi_0) = \arg \{1 + r e^{j\psi}\}, \quad (\text{B.3})$$

and a uniform bound in φ_0 follows from a bound on $\max_{\psi \in \mathbb{R}} |\arg(1 + r e^{j\psi})|$.

For notational convenience we therefore define

$$w = 1 + r e^{j\psi} = (1 + r \cos \psi) + j(r \sin \psi). \quad (\text{B.4})$$

If $0 \leq r < 1$, then $\operatorname{Re} w = 1 + r \cos \psi \geq 1 - r > 0$, hence $\arg w \in (-\pi/2, \pi/2)$ and $\sin(\cdot)$ is strictly increasing on $[0, \pi/2]$, and thus bounding $|\arg w|$ is equivalent to bounding $|\sin(\arg w)|$:

$$|\arg w| \leq \arcsin r \Leftrightarrow |\sin(\arg w)| \leq r. \quad (\text{B.5})$$

Using $\sin(\arg w) = \operatorname{Im}\{w\}/|w|$ we get

$$|\sin(\arg w)| = \frac{|r \sin \psi|}{\sqrt{(1 + r \cos \psi)^2 + (r \sin \psi)^2}} = \frac{r |\sin \psi|}{\sqrt{1 + r^2 + 2r \cos \psi}}. \quad (\text{B.6})$$

Substituting (B.6) into (B.5) and $|\sin(\arg w)| \leq r$ is equivalent to

$$|\sin \psi| \leq \sqrt{1 + r^2 + 2r \cos \psi}. \quad (\text{B.7})$$

If $r=0$ the bound is trivial. Squaring both sides gives

$$\sin^2 \psi \leq 1 + r^2 + 2r \cos \psi \Leftrightarrow 1 - \cos^2 \psi \leq 1 + r^2 + 2r \cos \psi \Leftrightarrow (\cos \psi + r)^2 \geq 0, \quad (\text{B.8})$$

which is always true. Hence $|\sin(\arg w)| \leq r$, and since $\arg w \in [-\pi/2, \pi/2]$ we conclude

$$|\arg w| \leq \arcsin r. \quad (\text{B.9})$$

Recalling $\delta_\theta(\varphi_0) = \arg w$ yields

$$|\delta_\theta(\varphi_0)| \leq \arcsin r. \quad (\text{B.10})$$

For the boundary case $r=1$, the same inequality implies $|\arg w| \leq \arcsin(1) = \pi/2$ whenever $w \neq 0$; at the isolated phases where $w=0$ (equivalently $F(\varphi_0)=0$) the argument is undefined and the bound is understood in the limiting sense.

Amplitude bound. From $F(\varphi_0) = G_+ + G_- e^{-j2\varphi_0}$ and the reverse triangle inequality,

$$|F(\varphi_0)| - |G_+| \leq |G_-|. \quad (\text{B.11})$$

Then applying the triangle inequality on the real line gives

$$|F(\varphi_0)| - 1 \leq |F(\varphi_0)| - |G_+| + |G_+| - 1 \leq |G_-| + |G_+| - 1. \quad (\text{B.12})$$

Since $\varepsilon_A(\varphi_0) = |F(\varphi_0)| - 1$, this is exactly the claimed bound. \square

B.2 Mean-square optimal scalar calibration

Proof of Theorem 2. Here and throughout, expectations are taken with respect to the distribution of window-level endpoint estimates (across windows, trials, or repetitions), not with respect to time within a single window. Assume finite second moments of Z, \hat{Z}

$$\mathbb{E}[|Z|^2] < \infty, \quad \mathbb{E}[|\hat{Z}|^2] < \infty, \quad \mathbb{E}[|\hat{Z}|^2] > 0 \quad (\text{B.13})$$

which excludes the degenerate case $\hat{Z} = 0$ almost surely.

The squared magnitude in (3.2) is expanded as

$$\begin{aligned} J(C) &= \mathbb{E}[(C\hat{Z} - Z)(C\hat{Z} - Z)^*] \\ &= \mathbb{E}[|C\hat{Z}|^2] - \mathbb{E}[C\hat{Z}Z^*] - \mathbb{E}[C^*\hat{Z}^*Z] + \mathbb{E}[|Z|^2]. \end{aligned} \quad (\text{B.14})$$

Linearity of expectation and the fact that C is deterministic lead to

$$J(C) = |C|^2 \mathbb{E}[|\hat{Z}|^2] - C \mathbb{E}[\hat{Z}Z^*] - C^* \mathbb{E}[\hat{Z}^*Z] + \mathbb{E}[|Z|^2]. \quad (\text{B.15})$$

Introducing the shorthand

$$\alpha = \mathbb{E}[|\hat{Z}|^2], \quad \beta = \mathbb{E}[\hat{Z}Z^*], \quad \gamma = \mathbb{E}[|Z|^2], \quad (\text{B.16})$$

gives the quadratic form

$$J(C) = \alpha|C|^2 - \beta C - \beta^*C^* + \gamma. \quad (\text{B.17})$$

Because $\alpha > 0$, the function J is strictly convex in C . Completion of the square yields

$$\begin{aligned} \alpha|C|^2 - \beta C - \beta^*C^* + \frac{|\beta|^2}{\alpha} &= \alpha \left[CC^* - C \frac{\beta}{\alpha} - C^* \frac{\beta^*}{\alpha} + \frac{\beta}{\alpha} \frac{\beta^*}{\alpha} \right] \\ &= \alpha \left| C - \frac{\beta}{\alpha} \right|^2. \end{aligned} \quad (\text{B.18})$$

Comparing with (B.17) using $\alpha \in \mathbb{R}$ gives

$$J(C) = \alpha \left| C - \frac{\beta}{\alpha} \right|^2 + \gamma - \frac{|\beta|^2}{\alpha}. \quad (\text{B.19})$$

The term $\alpha|C - \beta/\alpha|^2$ is nonnegative and equals zero if and only if

$$C = \frac{\beta}{\alpha} = \frac{\mathbb{E}[\hat{Z}Z^*]}{\mathbb{E}[|\hat{Z}|^2]}. \quad (\text{B.20})$$

This expression coincides with (3.3) and is therefore the unique minimiser of J . Evaluating J at $C = C_{\text{opt}}$ gives

$$J(C_{\text{opt}}) = \gamma - \frac{|\beta|^2}{\alpha} = \mathbb{E}[|Z|^2] - \frac{\left| \mathbb{E}[\hat{Z}Z^*] \right|^2}{\mathbb{E}[|\hat{Z}|^2]}, \quad (\text{B.21})$$

which is (3.4). Since C_{opt} is the global minimiser, $J(C_{\text{opt}}) \leq J(C)$ for all $C \in \mathbb{C}$. \square

B.3 Correlation form of the minimal MSE

Proof of Corollary 1. By the definition of $\rho_{Z\hat{Z}}$,

$$|\mathbb{E}[\hat{Z}^*Z]|^2 = |\rho_{Z\hat{Z}}|^2 \mathbb{E}[|\hat{Z}|^2] \mathbb{E}[|Z|^2]. \quad (\text{B.22})$$

Substitution into (3.4) yields

$$\begin{aligned} J(C_{\text{opt}}) &= \mathbb{E}[|Z|^2] - \frac{|\rho_{Z\hat{Z}}|^2 \mathbb{E}[|\hat{Z}|^2] \mathbb{E}[|Z|^2]}{\mathbb{E}[|\hat{Z}|^2]} \\ &= \mathbb{E}[|Z|^2] \left(1 - |\rho_{Z\hat{Z}}|^2 \right), \end{aligned} \quad (\text{B.23})$$

which is (3.6). The Cauchy-Schwarz inequality implies $|\rho_{Z\hat{Z}}| \leq 1$, hence $0 \leq 1 - |\rho_{Z\hat{Z}}|^2 \leq 1$ and

$$0 \leq J(C_{\text{opt}}) \leq \mathbb{E}[|Z|^2]. \quad (\text{B.24})$$

Equality $J(C_{\text{opt}}) = 0$ holds if and only if $|\rho_{Z\hat{Z}}| = 1$, which is equivalent to $\hat{Z} = CZ$ almost surely for some constant C . Equality $J(C_{\text{opt}}) = \mathbb{E}[|Z|^2]$ holds if and only if $\rho_{Z\hat{Z}} = 0$, i.e. \hat{Z} and Z are uncorrelated. \square

Corollary 1 shows that, after calibration, the minimal achievable mean-square error is entirely determined by the squared magnitude of the complex correlation coefficient between the ecHT endpoint \hat{Z} and the ideal analytic signal Z . The remaining error is equal to the signal power scaled by $(1 - |\rho_{Z\hat{Z}}|^2)$, which quantifies the fraction of signal energy that is fundamentally unrecoverable by

any linear calibration. Perfect correlation $|\rho_{Z\hat{Z}}|^2 = 1$ implies that calibration can fully correct the ecHT up to a constant complex gain, whereas zero correlation means that the ecHT output contains no usable information about the true signal. Thus, correlation (not calibration) sets the fundamental accuracy limit of the c-ecHT, and all sources of distortion impact performance only insofar as they reduce this correlation.

Geometrically, the calibrated estimate $C_{\text{opt}}\hat{Z}$ is the orthogonal projection of Z onto the one-dimensional subspace spanned by \hat{Z} in the Hilbert space of complex random variables, and $J(C_{\text{opt}})$ equals the squared norm of the irreducible projection residual. Equivalently, the factor $|\rho_{Z\hat{Z}}|^2$ represents the fraction of the analytic signal energy that is linearly recoverable from the ecHT output, while $1 - |\rho_{Z\hat{Z}}|^2$ quantifies the fundamental energy loss induced by filtering, windowing, and spectral leakage.

B.4 Bias-variance decomposition

For any scalar calibration C , the mean-square error admits the decomposition

$$J(C) = \mathbb{E}[C\hat{Z} - Z]^2 + \mathbb{E}\left[\left|(C\hat{Z} - Z) - \mathbb{E}[C\hat{Z} - Z]\right|^2\right], \quad (\text{B.25})$$

i.e. into a squared bias term and a variance term. The bias term captures the deterministic distortions caused by filter delay, amplitude mis-scaling, and systematic phase offsets. The variance term, on the other hand, measures the inconsistency in the estimate from one cycle to the next, which is caused by noise, spectral leakage and phase-dependent interference between positive and negative frequencies. The optimal calibration C_{opt} minimises both contributions jointly: it aligns the ecHT estimate with the ideal analytic signal as closely as possible on average, while also yielding the smallest possible endpoint variability of all scalar calibrations. Consequently, any further improvement beyond calibration must reduce either leakage or noise in the ecHT itself, as post-hoc scaling cannot reduce the residual variance below this limit.

Define the complex-valued endpoint error

$$e = C\hat{Z} - Z, \quad (\text{B.26})$$

so that

$$J(C) = \mathbb{E}[|C\hat{Z} - Z|^2] = \mathbb{E}[|e|^2]. \quad (\text{B.27})$$

Let

$$\mu = \mathbb{E}[e] = \mathbb{E}[C\hat{Z} - Z] \quad (\text{B.28})$$

denote the mean error. Then e can be written as

$$e = \mu + (e - \mu), \quad (\text{B.29})$$

where $e - \mu$ is a zero-mean fluctuation. Substituting this into $|e|^2$ yields

$$\begin{aligned} |e|^2 &= |\mu + (e - \mu)|^2 \\ &= (\mu + (e - \mu))(\mu + (e - \mu))^* \\ &= (\mu + (e - \mu))(\mu^* + (e - \mu)^*) \\ &= |\mu|^2 + |e - \mu|^2 + \mu^*(e - \mu) + \mu(e - \mu)^*. \end{aligned} \tag{B.30}$$

Taking expectations on both sides gives

$$\mathbb{E}[|e|^2] = \mathbb{E}[|\mu|^2] + \mathbb{E}[|e - \mu|^2] + \mathbb{E}[\mu^*(e - \mu)] + \mathbb{E}[\mu(e - \mu)^*]. \tag{B.31}$$

Since μ is deterministic, $\mathbb{E}[|\mu|^2] = |\mu|^2$. Moreover,

$$\mathbb{E}[\mu^*(e - \mu)] = \mu^* \mathbb{E}[e - \mu] = \mu^*(\mathbb{E}[e] - \mu) = \mu^*(\mu - \mu) = 0, \tag{B.32}$$

and similarly $\mathbb{E}[\mu(e - \mu)^*] = 0$, because $\mathbb{E}[e - \mu] = 0$ by construction. Hence

$$\mathbb{E}[|e|^2] = |\mu|^2 + \mathbb{E}[|e - \mu|^2]. \tag{B.33}$$

Substituting back $e = C\hat{Z} - Z$ and $\mu = \mathbb{E}[C\hat{Z} - Z]$ yields the bias-variance decomposition

$$\begin{aligned} J(C) &= \mathbb{E} \left[|C\hat{Z} - Z|^2 \right] \\ &= |\mathbb{E}[C\hat{Z} - Z]|^2 + \mathbb{E} \left[|(C\hat{Z} - Z) - \mathbb{E}[C\hat{Z} - Z]|^2 \right]. \end{aligned} \tag{B.34}$$

B.5 Large-sample properties of the empirical calibration

We estimate the optimal scalar calibration

$$C_{\text{opt}} = \frac{\mathbb{E}[\hat{Z}^* Z]}{\mathbb{E}[|\hat{Z}|^2]} \tag{B.35}$$

from M consecutive windows. Because windows are extracted from a time series, the resulting sequence $\{(Z_i, \hat{Z}_i)\}_{i \geq 1}$ is typically not iid; neighbouring windows may be correlated. The goal is to state conditions under which the ratio estimator

$$\hat{C}_M = \frac{\frac{1}{M} \sum_{i=0}^{M-1} \hat{Z}_i^* Z_i}{\frac{1}{M} \sum_{i=0}^{M-1} |\hat{Z}_i|^2} \tag{B.36}$$

is (1) consistent and (2) asymptotically normal as $M \rightarrow \infty$.

Define

$$A_i = \hat{Z}_i^* Z_i, \quad B_i = |\hat{Z}_i|^2, \quad \bar{A}_M = \frac{1}{M} \sum_{i=0}^{M-1} A_i, \quad \bar{B}_M = \frac{1}{M} \sum_{i=0}^{M-1} B_i, \tag{B.37}$$

so that $\hat{C}_M = \bar{A}_M/\bar{B}_M$ and $C_{\text{opt}} = \mathbb{E}[A_1]/\mathbb{E}[B_1]$.

These assumptions are intended for window-level features (Z_i, \hat{Z}_i) , not raw samples: each window aggregates many samples, so correlations between widely separated windows are typically weaker than correlations between adjacent raw samples.

- (i) **Strict stationarity** $\{(A_i, B_i)\}$ is invariant under time shifts (e.g. $\mathbb{E}[A_i] = \mathbb{E}[A_1]$ and $\mathbb{E}[B_i] = \mathbb{E}[B_1]$). This ensures $\mathbb{E}[A_i]$ and $\mathbb{E}[B_i]$ do not depend on i , i.e. the target C_{opt} is time-invariant.
- (ii) **Ergodicity** Time averages converge to ensemble averages. Concretely, ergodicity delivers a law of large numbers for dependent data, so $\bar{A}_M \rightarrow \mathbb{E}[A_1]$ and $\bar{B}_M \rightarrow \mathbb{E}[B_1]$ even without independence.
- (iii) **Weak dependence/Strong mixing** Dependence between windows decays with lag. This is not needed to define C_{opt} but it is what enables a central limit theorem (CLT) and therefore uncertainty quantification for \hat{C}_M .
- (iv) **Finite moments and non-degeneracy** $\mathbb{E}[A_1] < \infty$, $\mathbb{E}[B_1] < \infty$, and $\mathbb{E}[B_1] > 0$. The first two conditions ensure integrability. The last condition prevents a denominator in the derivation from collapsing and guarantees the ration map is well behaved near the limit.
- (v) **Higher moments** $\mathbb{E}[|A_1|^{2+\delta}] < \infty$ and $\mathbb{E}[|B_1|^{2+\delta}] < \infty$ for some $\delta > 0$.

Define the empirical calibration based on M windows by

$$\hat{C}_M = \frac{\frac{0}{M-1} \sum_{i=1}^M \hat{Z}_i^* Z_i}{\frac{0}{M-1} \sum_{i=1}^M |\hat{Z}_i|^2} = \frac{\bar{A}_M}{\bar{B}_M}, \quad (\text{B.38})$$

and let

$$C_{\text{opt}} = \frac{\mathbb{E}[\hat{Z}^* Z]}{\mathbb{E}[|\hat{Z}|^2]} = \frac{\mathbb{E}[A_1]}{\mathbb{E}[B_1]} \quad (\text{B.39})$$

denote the theoretical MSE-optimal scalar calibration.

Proof of Corollary 2. (1) Consistency (almost sure convergence). By assumption, the sequence $\{(A_i, B_i)\}_{i \geq 1}$ is strictly stationary (i) and ergodic (ii). Because the sequence is stationary and ergodic and integrable, sample averages of A_i and B_i converge almost surely to their expectations, the strong law of large numbers for such processes implies

$$\bar{A}_M \xrightarrow{\text{a.s.}} \mathbb{E}[A_1], \quad \bar{B}_M \xrightarrow{\text{a.s.}} \mathbb{E}[B_1], \quad (\text{B.40})$$

as $M \rightarrow \infty$, provided the first moments are finite (iv). Ergodicity and suitable weak dependence is sufficient to ensure time averages converge to expectations.

Assumption (iv) includes $\mathbb{E}[B_1] > 0$. Since $\bar{B}_M \rightarrow \mathbb{E}[B_1]$ almost surely, once \bar{B}_M is sufficiently close to $\mathbb{E}[B_1]$, it must be positive and bounded away from zero almost surely. Formally, there exists an M_0 such that for all $M \geq M_0$,

$$|\bar{B}_M - \mathbb{E}[B_1]| < \frac{1}{2}\mathbb{E}[B_1]. \quad (\text{B.41})$$

Then for those M ,

$$\bar{B}_M \geq \frac{1}{2}\mathbb{E}[B_1] > 0. \quad (\text{B.42})$$

So the ratio \bar{A}_M/\bar{B}_M is eventually well-defined and stable.

An algebraic bound can be found

$$\hat{C}_M - C_{\text{opt}} = \frac{\bar{A}_M}{\bar{B}_M} - \frac{\mu_A}{\mu_B} = \frac{\mu_B(\bar{A}_M - \mu_A) - \mu_A(\bar{B}_M - \mu_B)}{\bar{B}_M \mu_B}, \quad (\text{B.43})$$

where $\mu_A = \mathbb{E}[A_1]$, $\mu_B = \mathbb{E}[B_1]$. The numerator converges to zero due to (B.40), and (B.42) ensures a finite denominator. This proves the empirical calibration is a strongly consistent estimator of C_{opt} .

(2) *Asymptotic normality.* Under assumptions (i), (iii) and (v), a multivariate central limit theorem for weakly dependent stationary sequences applies to the real-valued vector process. (i) ensures stationary sequences, (iii) is the main assumption enabling the CLT with rate \sqrt{M} and a well-defined covariance, (v) ensures the mixing CLT applies and the long-run covariance exists.

$$\mathbf{Y}_i = \begin{pmatrix} \text{Re } A_i \\ \text{Im } A_i \\ B_i \end{pmatrix}, \quad \bar{\mathbf{Y}}_M = \frac{1}{M} \sum_{i=0}^{M-1} \mathbf{Y}_i \quad (\text{B.44})$$

Weak dependence plus a $2 + \delta$ moment condition allow a multivariate CLT for $\bar{\mathbf{Y}}_M$ with a long-run covariance Σ_Y that captures serial correlation, assuming the series converges. In the iid case, this reduces to $\Sigma_Y = \text{Cov}(\mathbf{Y}_1)$.

$$\sqrt{M}(\bar{\mathbf{Y}}_M - \mathbb{E}[\mathbf{Y}_1]) \xrightarrow{d} \mathcal{N}(\mathbf{0}, \Sigma_Y), \quad \Sigma_Y = \sum_{l \in \mathbb{Z}} \text{Cov}(\mathbf{Y}_1, \mathbf{Y}_{1+l}). \quad (\text{B.45})$$

From the definitions,

$$\bar{A}_M = \bar{Y}_{M,1} + j\bar{Y}_{M,2}, \quad \bar{B}_M = \bar{Y}_{M,3}. \quad (\text{B.46})$$

Hence the estimator is not linear, but a smooth function of means,

$$\hat{C}_M = \frac{\bar{A}_M}{\bar{B}_M} = \frac{\bar{Y}_{M,1} + j\bar{Y}_{M,2}}{\bar{Y}_{M,3}}. \quad (\text{B.47})$$

The delta method replaces a smooth nonlinear function by its first-order Taylor expansion around the mean, so asymptotically the estimator behaves like a

linear function of a Gaussian vector [35]. In this way, the empirical calibration \hat{C}_M can be written as a smooth function of $\bar{\mathbf{Y}}_M$. For this purpose, we define a real mapping $f: \mathbb{R}^3 \rightarrow \mathbb{R}^2$ that outputs real and imaginary parts.

$$f(x, y, b) = \begin{pmatrix} x/b \\ y/b \end{pmatrix} \quad (\text{B.48})$$

Then $f(\bar{\mathbf{Y}}_M) = (\text{Re } \hat{C}_M, \text{Im } \hat{C}_M)$ and using its Taylor series. By assumption (iv) $\mu_B = \mathbb{E}[B_1] > 0$ ensures that f is differentiable in a neighbourhood of $\boldsymbol{\mu}$.

$$f(\bar{\mathbf{Y}}_M) \approx f(\boldsymbol{\mu}) + \mathbf{J}_f(\boldsymbol{\mu})(\bar{\mathbf{Y}}_M - \boldsymbol{\mu}) \quad (\text{B.49})$$

Multiplying by \sqrt{M} , we obtain

$$\sqrt{M}(f(\bar{\mathbf{Y}}_M) - f(\boldsymbol{\mu})) \approx \mathbf{J}_f(\boldsymbol{\mu})\sqrt{M}(\bar{\mathbf{Y}}_M - \boldsymbol{\mu}). \quad (\text{B.50})$$

Since the right-hand side converges to a Gaussian, so does the left-hand side.

Computing the Jacobian $\mathbf{J}_f(\boldsymbol{\mu})$ with $\boldsymbol{\mu} = \mathbb{E}[\mathbf{Y}_1] = (\mu_x, \mu_y, \mu_B)$ and $\mu_B = \mathbb{E}[B_1] > 0$ yields

$$\mathbf{J}_f(\boldsymbol{\mu}) = \begin{pmatrix} \frac{\partial}{\partial x} \frac{x}{b} & \frac{\partial}{\partial y} \frac{x}{b} & \frac{\partial}{\partial b} \frac{x}{b} \\ \frac{\partial}{\partial x} \frac{y}{b} & \frac{\partial}{\partial y} \frac{y}{b} & \frac{\partial}{\partial b} \frac{y}{b} \end{pmatrix} = \begin{pmatrix} \frac{1}{\mu_B} & 0 & -\frac{\mu_x}{\mu_B^2} \\ 0 & \frac{1}{\mu_B} & -\frac{\mu_y}{\mu_B^2} \end{pmatrix}. \quad (\text{B.51})$$

If (B.45) and f is differentiable in $\boldsymbol{\mu}$,

$$\sqrt{M}(f(\bar{\mathbf{Y}}_M) - f(\boldsymbol{\mu})) \xrightarrow{d} \mathcal{N}(\mathbf{0}, \mathbf{J}_f \boldsymbol{\Sigma}_Y \mathbf{J}_f^\top). \quad (\text{B.52})$$

But $f(\boldsymbol{\mu}) = (\mu_x/\mu_B, \mu_y/\mu_B)$, which is exactly $(\text{Re } C_{\text{opt}}, \text{Im } C_{\text{opt}})$ because $\mu_x + j\mu_y = \mathbb{E}[A_1]$ and $\mu_B = \mathbb{E}[B_1]$. Also $f(\bar{\mathbf{Y}}_M) = (\text{Re } \hat{C}_M, \text{Im } \hat{C}_M)$. Therefore,

$$\sqrt{M} \begin{pmatrix} \text{Re}\{\hat{C}_M - C_{\text{opt}}\} \\ \text{Im}\{\hat{C}_M - C_{\text{opt}}\} \end{pmatrix} \xrightarrow{d} \mathcal{N}(\mathbf{0}, \boldsymbol{\Sigma}_C), \quad \boldsymbol{\Sigma}_C = \mathbf{J}_f(\boldsymbol{\mu}) \boldsymbol{\Sigma}_Y \mathbf{J}_f(\boldsymbol{\mu})^\top \quad (\text{B.53})$$

Finally, since a complex number is equivalent to its 2D real vector $(\text{Re } \cdot, \text{Im } \cdot)$, the above 2D real CLT can be summarised as

$$\sqrt{M} (\hat{C}_M - C_{\text{opt}}) \xrightarrow{d} \mathcal{N}_{\mathbb{C}}(\mathbf{0}, \boldsymbol{\Sigma}_C). \quad (\text{B.54})$$

In particular, the variance of \hat{C}_M decreases at the rate of $1/M$, and the real and imaginary parts of the calibration error are asymptotically jointly Gaussian. \square

As mentioned previously, the assumptions of this derivation are not intended to model raw samples. Instead, the sequence $\{(Z_i, \hat{Z}_i)\}$ is formed from *window-level endpoint estimates*, which aggregate many raw samples into a single complex-valued quantity. For band-limited, approximately stationary signals, such window-level features can be well approximated by stationary, weakly

dependent processes over short lengths [36], [37], [38], [39]. In this setting, the *effective* number of independent observations is determined by the number of usable windows M rather than by the raw sampling rate. The above theorem states that the empirical calibration converges to the optimal Wiener gain and that its estimation error decays as $1/\sqrt{M}$ even in the presence of temporal correlations typical of EEG data.

B.6 Optimal scalar calibration for a single tone

For the finite length cosine analysed in section 2.5, the ecHT endpoint obeys

$$F = G_+ + G_- e^{-j2\varphi_0}, \quad (\text{B.55})$$

where G_+ is the effective complex gain for the positive-frequency component and G_- the effective gain (leakage) for the negative-frequency component. The initial phase φ_0 is modelled as random with $\varphi_0 \sim \mathcal{U}(-\pi, \pi)$ to represent an unknown phase offset.

The average error over all possible initial phase offsets can be stated to get an expected error that does not depend on the arbitrary phase of the input signal. No closed-form solution exists for these integrals, but they can be evaluated numerically.

$$\bar{\varepsilon}_\theta = \mathbb{E}[\varepsilon_\theta] = \frac{1}{2\pi} \int_{-\pi}^{\pi} \arg F d\varphi_0 \quad (\text{B.56})$$

$$\bar{\varepsilon}_A = \mathbb{E}[\varepsilon_A] = \frac{1}{2\pi} \int_{-\pi}^{\pi} |F| - 1 d\varphi_0 \quad (\text{B.57})$$

The mean-squared error can also be stated directly since $\mathbb{E} e^{\pm j2\varphi_0} = 0$.

$$\begin{aligned} \text{MSE} &= \mathbb{E}|F - 1|^2 \\ &= \mathbb{E} \left[|G_+ - 1|^2 + |G_-|^2 + (G_+ - 1)G_-^* e^{j2\varphi_0} + (G_+ - 1)^*G_- e^{-j2\varphi_0} \right] \\ &= |G_+ - 1|^2 + |G_-|^2 \end{aligned} \quad (\text{B.58})$$

$|G_+ - 1|^2$ contributes from systematic distortion of the main (positive) component and $|G_-|^2$ contributes leakage from the negative component. The general result from Section 3.1 is specialised in this section.

Under the assumptions above, the MSE-optimal scalar calibration factor (3.3) specialises to

$$C_{\text{opt}} = \frac{G_+^*}{|G_+|^2 + |G_-|^2}. \quad (\text{B.59})$$

The corresponding minimal mean-square error is

$$J(C_{\text{opt}}) = \frac{|G_-|^2}{|G_+|^2 + |G_-|^2}. \quad (\text{B.60})$$

Proof of Theorem 3. Since $\hat{Z} = FZ$ and $|Z| = 1$, it follows that

$$\hat{Z}^*Z = F^*, \quad |\hat{Z}|^2 = |F|^2. \quad (\text{B.61})$$

Taking expectations with respect to φ_0 ,

$$\mathbb{E}[\hat{Z}^*Z] = \mathbb{E}[F^*] = \mathbb{E}[G_+^* + G_-^* e^{j2\varphi_0}] = G_+^*, \quad (\text{B.62})$$

because $\mathbb{E}[e^{\pm j2\varphi_0}] = 0$ for $\varphi_0 \sim \mathcal{U}(-\pi, \pi)$. Furthermore,

$$\begin{aligned} \mathbb{E}[|\hat{Z}|^2] &= \mathbb{E}[|F|^2] = \mathbb{E}[|G_+ + G_- e^{-j2\varphi_0}|^2] \\ &= \mathbb{E}\left[|G_+|^2 + |G_-|^2 + G_+ G_-^* e^{j2\varphi_0} + G_+^* G_- e^{-j2\varphi_0}\right] \\ &= |G_+|^2 + |G_-|^2. \end{aligned} \quad (\text{B.63})$$

Insertion into (3.3) yields

$$C_{\text{opt}} = \frac{\mathbb{E}[\hat{Z}^*Z]}{\mathbb{E}[|\hat{Z}|^2]} = \frac{G_+^*}{|G_+|^2 + |G_-|^2}, \quad (\text{B.64})$$

which is (3.11). For the minimal MSE, (3.4) is used with $\mathbb{E}[|Z|^2] = 1$:

$$\begin{aligned} J(C_{\text{opt}}) &= 1 - \frac{\mathbb{E}[\hat{Z}^*Z]}{\mathbb{E}[|\hat{Z}|^2]} \\ &= 1 - \frac{|G_+|^2}{|G_+|^2 + |G_-|^2} = \frac{|G_-|^2}{|G_+|^2 + |G_-|^2}, \end{aligned} \quad (\text{B.65})$$

which proves (3.12). \square

Thus, for a single cosine tone the best scalar calibration depends only on the positive-frequency gain G_+ and the negative-frequency leakage G_- , and the minimal achievable MSE is exactly the fraction of leakage power $|G_-|^2$ in the total ecHT endpoint power $|G_+|^2 + |G_-|^2$. The coefficient C_{opt} coincides with the scalar Wiener filter that produces the linear minimum-variance estimate of Z from the observation \hat{Z} in the single-tone setting.

The corresponding correlation coefficient and deterministic bounds on phase and amplitude error can also be expressed explicitly.

$$\rho_{Z\hat{Z}} = \frac{\mathbb{E}[\hat{Z}^*Z]}{\sqrt{\mathbb{E}[|\hat{Z}|^2] \mathbb{E}[|Z|^2]}} = \frac{G_+^*}{\sqrt{|G_+|^2 + |G_-|^2}}, \quad (\text{B.66})$$

so that

$$|\rho_{Z\hat{Z}}|^2 = \frac{|G_+|^2}{|G_+|^2 + |G_-|^2}, \quad (\text{B.67})$$

and the minimal MSE (3.12) can be written as

$$J(C_{\text{opt}}) = 1 - |\rho_{Z\hat{Z}}|^2. \quad (\text{B.68})$$

Thus, the leakage power $|G_-|^2$ directly reduces the squared correlation between the ecHT endpoint and the ideal analytic endpoint, and therefore limits the minimal achievable MSE.

B.7 Bounding the noise gain

Recall that the ecHT endpoint at $n = N - 1$ is a linear functional of the windowed samples. Hence there exists an endpoint impulse response $\mathbf{h} = (h_0, \dots, h_{N-1})^\top \in \mathbb{C}^N$ such that, for any real (or complex) input $x(n)$,

$$\hat{z}_{\text{end}} = \sum_{n=0}^{N-1} h_n x(n). \quad (\text{B.69})$$

If $\eta(n)$ is zero-mean white noise with variance $\mathbb{E}[|\eta(n)|^2] = \sigma_\eta^2$, the corresponding noise contribution at the endpoint is

$$W = \sum_{n=0}^{N-1} h_n \eta(n), \quad \sigma_W^2 = \mathbb{E}[|W|^2] = \sigma_\eta^2 \sum_{n=0}^{N-1} |h_n|^2, \quad (\text{B.70})$$

so that the noise gain can be written as

$$G_{\text{noise}} = \frac{\sigma_W^2}{\sigma_\eta^2} = \sum_{n=0}^{N-1} |h_n|^2. \quad (\text{B.71})$$

Moreover, up to deterministic phase factors of unit modulus (which do not affect squared magnitudes), the single-tone endpoint gains $G_{+,-}$ correspond to the response of the same linear functional to complex exponentials at frequencies $\pm\omega_0$, and can be written as

$$G_+ = \sum_{n=0}^{N-1} h_n e^{-j\omega_0 n}, \quad G_- = \sum_{n=0}^{N-1} h_n e^{+j\omega_0 n}. \quad (\text{B.72})$$

Equivalently, $G_\pm = \mathbf{h}^\top \mathbf{v}_\pm$ with $\mathbf{v}_\pm = e^{\mp j\omega_0 n}$ are the inner products of \mathbf{h} with the vectors $\mathbf{v}_\pm \in \mathbb{C}^N$ whose Euclidean norms satisfy $\|\mathbf{v}_+\|_2^2 = \|\mathbf{v}_-\|_2^2 = N$.

Corollary 3 (Noise gain vs. single-tone gains). *For any fixed ecHT design with endpoint impulse response h ,*

$$G_{\text{noise}} \geq \frac{|G_+|^2 + |G_-|^2}{2N}. \quad (\text{B.73})$$

Proof. By Cauchy-Schwarz,

$$|G_+| = |\langle \mathbf{h}, \mathbf{v}_+ \rangle| \leq \|\mathbf{h}\|_2 \|\mathbf{v}_+\|_2 = \sqrt{G_{\text{noise}}} \sqrt{N}, \quad (\text{B.74})$$

and similarly $|G_-| \leq \sqrt{G_{\text{noise}}} \sqrt{N}$. Squaring and adding the two inequalities yields

$$|G_+|^2 + |G_-|^2 \leq 2N G_{\text{noise}}, \quad (\text{B.75})$$

which is equivalent to the stated bound. \square

In terms of the leakage ratio $r = |G_-|/|G_+|$, the bound can be written as

$$G_{\text{noise}} \geq \frac{|G_+|^2}{2N} (1 + r^2). \quad (\text{B.76})$$

For typical ecHT designs one has $r \ll 1$ and $|G_+| \approx 1$, so the noise gain cannot be much smaller than $|G_+|^2/(2N)$; that is, the endpoint noise power is bounded below by the main-lobe gain squared, averaged over the effective N degrees of freedom of the window.

C Discussion of argument function

There are two natural but not equivalent ways to define the instantaneous phase from the analytic signal.

C.1 Method 1: phase of the analytic signal

The first definition takes the phase directly as the argument of the complex analytic signal.

$$z(n) = x(n) + j\mathcal{H}x(n), \quad (\text{C.1})$$

$$\theta_1(n) = \arg z(n) = \arctan2(\text{Im } z(n), \text{Re } z(n)). \quad (\text{C.2})$$

The endpoint value can be written as

$$\hat{z}_{\text{end}} = z_{\text{end}} F \quad (\text{C.3})$$

where

$$z_{\text{end}} = e^{j(\omega_0(N-1)+\varphi_0)} \quad (\text{C.4})$$

is the ideal analytic signal of the cosine at the endpoint and F is the effective complex gain that collects the effects of finite windowing (Dirichlet kernel), analytic masking and bandpass filtering (see Section 2.5). Hence

$$\begin{aligned} \theta_1(N-1) &= \arg \hat{z}_{\text{end}} \\ &= \arg \{z_{\text{end}} F\} \\ &= \omega_0(N-1) + \varphi_0 + \arg F. \end{aligned} \quad (\text{C.5})$$

Thus, Method 1 preserves the linear phase progression $\omega_0 n + \varphi_0$ of the tone and only adds a phase error $\arg F$ which decomposes into a calibratable bias $\arg G_+$ and a phase-dependent ripple bounded by $\arcsin r$.

C.2 Method 2: phase from the ratio to the original signal

A second definition, which has also appeared in the ecHT literature, replaces the real part of the analytic signal in the denominator by the original signal $x(n)$:

$$\theta_2(n) = \arctan2(\operatorname{Im} z(n), x(n)). \quad (\text{C.6})$$

For an ideal analytic signal, $\operatorname{Re} z(n) = x(n)$, so $\theta_1(n) = \theta_2(n)$. However, finite windowing and bandpass filtering distort the real and imaginary parts of $z(n)$ relative to the original signal. Using the endpoint representation

$$\hat{z}_{\text{end}} = z_{\text{end}}F \quad (\text{C.7})$$

$$z_{\text{end}} = \cos \psi + j \sin \psi \quad (\text{C.8})$$

$$\psi = \omega_0(N - 1) + \varphi_0. \quad (\text{C.9})$$

Multiplying out the product using $F = F_R + jF_I$

$$\begin{aligned} \hat{z}_{\text{end}} &= (\cos \psi + j \sin \psi)(F_R + jF_I) \\ &= F_R \cos \psi + jF_R \sin \psi + jF_I \cos \psi - F_I \sin \psi, \end{aligned} \quad (\text{C.10})$$

one obtains

$$\operatorname{Re} \hat{z}_{\text{end}} = F_R \cos \psi - F_I \sin \psi, \quad (\text{C.11})$$

$$\operatorname{Im} \hat{z}_{\text{end}} = F_R \sin \psi + F_I \cos \psi. \quad (\text{C.12})$$

Using $\operatorname{Re} z_{\text{end}} = \cos \psi$, Method 2 yields

$$\tan \theta_2(N - 1) = \frac{\operatorname{Im} \hat{z}_{\text{end}}}{x_{\text{end}}} = \frac{F_R \sin \psi + F_I \cos \psi}{\cos \psi} = F_R \tan \psi + F_I. \quad (\text{C.13})$$

Consequently,

$$\theta_2(N - 1) = \arctan2(F_R \sin \psi + F_I \cos \psi, \cos \psi), \quad (\text{C.14})$$

which is a nonlinear function of n (through $\psi = \omega_0(N - 1) + \varphi_0$) and of the initial phase φ_0 . This shows that the effective ecHT gain F causes a rotation and non-uniform scaling of the cosine-sine quadrature pair. In the ideal case $F = 1$, the real and imaginary components recover the standard analytic signal representation.

In contrast to Method 1, the phase evolution is no longer strictly linear, but warped by F which includes filter and window effects. For this reason, Method 2 is not recommended for ecHT phase estimation. In this work, Method 1 will be used exclusively.